

Chandra Observations of Gas Stripping and Nuclear Outflows in the Elliptical Galaxy NGC 4552 in the Virgo Cluster

M. Machacek, C. Jones, W. R. Forman, and P. Nulsen¹

Harvard-Smithsonian Center for Astrophysics

60 Garden Street, Cambridge, MA 02138 USA

mmachacek@cfa.harvard.edu

ABSTRACT

We use a 54.4 ks *Chandra* observation to study ram-pressure stripping and nuclear outflow activity in NGC 4552 (M89), an elliptical galaxy in the Virgo Cluster. *Chandra* images in the 0.5 – 2 keV band show a sharp leading edge in the surface brightness 3.1 kpc north of the galaxy center, a cool ($kT = 0.51^{+0.09}_{-0.06}$ keV) tail with mean density $n_e \sim 5.4 \pm 1.7 \times 10^{-3}$ cm $^{-3}$ extending ~ 10 kpc to the south of the galaxy, and two 3–4 kpc horns of emission extending southward away from the leading edge. These are all features characteristic of supersonic ram-pressure stripping of galaxy gas, due to NGC 4552’s motion through the surrounding Virgo ICM. Fitting the surface brightness profile and spectra across the leading edge, we find the galaxy gas inside the edge is cooler ($kT = 0.43^{+0.02}_{-0.03}$ keV) and denser ($n_e \sim 0.010$ cm $^{-3}$) than the surrounding Virgo ICM ($kT = 2.2^{+0.6}_{-0.4}$ keV and $n_e = 3.0 \pm 0.3 \times 10^{-4}$ cm $^{-3}$). The resulting pressure ratio between the free-streaming ICM and cluster gas at the stagnation point is $\sim 7 \pm 1.4$ for galaxy gas metallicities of $0.6^{+0.4}_{-0.2} Z_\odot$, which suggests that NGC 4552 is moving supersonically through the cluster with a speed $v \sim 1610 \pm 150$ km s $^{-1}$ (Mach 2.1 ± 0.2) at an angle $\xi \sim 37^{+5}_{-4}$ towards us with respect to the plane of the sky. *Chandra* images also show two ring-like features ~ 1.7 kpc in diameter in the core of NGC 4552, as reported previously by Filho et al. We use spherically symmetric point explosion shock models to argue that the shape of the surface brightness profile across the rims of the rings and the temperature of hot gas in the rings are consistent with a Mach 1.7 shock carrying mean mechanical power $L_{\text{mech}} \sim 3 \times 10^{41}$ erg s $^{-1}$ produced by a $\sim 1.4 \times 10^{55}$ erg nuclear outburst $\sim 1 - 2$ Myr ago.

Subject headings: galaxies: clusters: general – galaxies: individual (NGC 4552, M89) – galaxies: intergalactic medium – X-rays: galaxies

1. INTRODUCTION

Hierarchical models of structure formation, in which galaxies formed at high redshift and rapidly coalesced into groups and clusters through accretion and mergers, have become a compelling paradigm for understanding galaxy evolution. In such dynamically rich environments, galaxies are subject to an array of physical processes that affect their evolution. These physical processes form two broad classes: (1) tidal interactions

such as those induced by major mergers (e.g., Lavery & Henry 1988), off-axis galaxy collisions (Müller et al. 1989), galaxy harassment (Moore et al. 1996) or galaxy fly-bys near the core of the cluster potential (Byrd & Valtonen 1990), and (2) gas-gas interactions, notably ram pressure by the intracluster gas (ICM) on the galaxy’s interstellar medium (ISM), due to the galaxy’s motion through the surrounding ICM (Gunn & Gott 1972), or ISM-ISM interactions produced in galaxy-galaxy collisions (Kenney et al. 1995). These gas-dynamical processes may be enhanced by turbulence and viscous effects (Nulsen 1982;

¹on leave from the University of Wollongong

Quilis et al. 2000) or inhomogeneities and bulk motions in the ICM gas (Kenney et al. 2004). Combes (2004) and references therein provide a recent overview. No model for galaxy evolution can be complete without a detailed understanding of the gas-dynamics of these interactions. Similarly no model for the evolution of the intracluster medium can be complete without understanding the feedback of gas and energy from the galaxy into the ICM by stripping processes and nuclear outflows induced by starbursts or jets from AGN.

The actions of tidal forces are identified by the appearance of disturbed stellar morphologies, such as stretched stellar tails (see e.g. Gnedin 2003, Vollmer 2003); while the characteristic signatures of hydrodynamic stripping (see e.g. Stevens et al. 1999; Toniazzo & Schindler 2001; Acreman et al. 2003 and references therein) and outflows (see e.g. Heinz, Reynolds, & Begelman 1998; Churazov et al. 2001; Quilis et al. 2001; Brüggen & Kaiser 2002; Omma et al. 2004 and references therein) are imprinted on the structure of the hot X-ray emitting gas in and near the galaxy. Notably the ram-pressure experienced by galaxies moving through the dense ICM near a group or cluster core can produce sharp surface brightness edges along the leading interface between the galaxy and the ICM. These are galaxy-sized analogues of subcluster-scale cold fronts, regions forming the boundaries between cool gas clouds moving through hot ambient gas in rich clusters during cluster mergers as smaller systems fall into the cluster, where a sharp rise in surface brightness (density) is accompanied by a corresponding drop in temperature (see, e.g. Markevitch et al. 2000, Vikhlinin et al. 2001; Mazzotta et al. 2001). The higher pressure found in the cold front compared to that in the cluster gas is balanced by the ram pressure caused by the motion of the cloud through the surrounding ICM. Tails of stripped galaxy gas are found to extend 10 to 200 kpc behind the galaxy before fading into the background emission of the ambient cluster gas (see e.g. Forman et al. 1979, White et al. 1991, Rangarajan et al. 1995 for M86; Irwin & Sarazin 1996, Biller et al. 2004 for NGC 4472; Sakelliou et al. 1996 for 4C34.16; Wang et al. 2004 for C153; Machacek et al. 2005a, Scharf et al. 2004 for NGC 1404). Detailed studies of these X-ray features in nearby systems (see, for example, Biller et al. 2004;

Machacek et al. 2005a, 2005b; Sun & Vikhlinin 2005; Sun, Jerius & Jones 2005), made possible by the high angular resolution of *Chandra* and *XMM-Newton*, not only reveal the nature of the gas-dynamics of the stripping process, but also are one of the few ways to constrain the three dimensional motion of the galaxy as it passes through the group or cluster core (Merrifield 1998; Dosaj et al. 2002).

NGC 4552 ($\alpha = 12^h35^m39.8^s, \delta = 12^\circ33'23''$, J2000) is an elliptical galaxy located 72' east of M87 in subcluster A of the Virgo cluster. Measurement of NGC 4552's distance modulus using surface brightness fluctuations (Tonry et al. 2001) places it at nearly the same luminosity distance as M87, while NGC 4552's low line of sight velocity ($v_r = 340 \pm 4 \text{ km s}^{-1}$, NED; Smith et al. 2000) compared to that of M87 ($v_r = 1307 \pm 7 \text{ km s}^{-1}$, NED; Smith et al. 2000) implies that NGC 4552 is moving supersonically through the Virgo ICM with at least $\Delta v_r = -967 \pm 11 \text{ km s}^{-1}$ towards us relative to M87. Thus NGC 4552 is a likely candidate for ram-pressure stripping by the cluster gas.

Since NGC 4552 is a member of the large sample of nearby elliptical galaxies used to establish correlations between X-ray emission and other ISM tracers (see e.g. O'Sullivan et al. 2001 and references therein), its global X-ray properties are well studied. Early observations with the *Einstei*n Observatory (Forman, Jones & Tucker 1985; Canizares, Fabbiano & Trinchieri 1987; Roberts et al. 1991; Kim, Fabbiano, & Trinchieri 1992; Eskridge, Fabbiano, & Kim 1995) focused on the measurement of NGC 4552's total X-ray luminosity to establish the $L_X - L_B$ relation. Subsequent *ROSAT* observations of NGC 4552 were used to study the possible dependence of this relation on environment (Brown & Bregman 2000; O'Sullivan et al. 2001). Fits to the mean X-ray spectrum for NGC 4552 using *ROSAT* resulted in mean temperatures for the X-ray gas in the galaxy of $\sim 0.5 - 0.8 \text{ keV}$ depending on the spectral model (Davis & White 1996; Brown & Bregman 2000; Matsushita 2001). Using *ASCA* data, Matsushita, Ohashi, & Makishima (2000) modelled the mean spectrum of NGC 4552 using variable abundance thermal plasma models and emphasized the importance of including an additional bremsstrahlung component in the spectral models to account for the contribution of unresolved X-ray

binaries in low spatial resolution data. They found mean temperatures ~ 0.6 keV for NGC 4552, in agreement with the *ROSAT* studies, but with generally higher abundances ($\gtrsim 0.4 Z_{\odot}$).

Most recent studies, across a wide range of wavelengths, have concentrated on the nuclear properties of NGC 4552. From optical line ratios, Ho et al. (1997) classify NGC 4552 as a LINER/HII transition object, possessing spectral properties of a low luminosity AGN contaminated by nearby star-forming HII regions. Radio continuum measurements taken with the VLA at 8.4 GHz (Filho, Barthel & Ho 2000) and with the VLBA at 5 GHz (Nagar et al. 2002) show a ~ 100 mJy core radio source, unresolved on milliarcsecond scales, at the galaxy center. Properties of the radio spectrum indicate a nonthermal origin for this radio emission, associated with accretion onto a central black hole (Nagar et al. 2002, Filho et al. 2004). From the correlation between the black hole mass and central velocity dispersion (Ferrarese & Merritt 2000; Gebhard et al. 2000), the mass of the central black hole in NGC 4552 is inferred to be $4 \times 10^8 M_{\odot}$. In recent *Chandra* X-ray observations, Filho et al. (2004) identified a hard X-ray source, whose X-ray spectrum is well represented by a $\Gamma = 1.51$ power law component plus a $kT = 0.95$ keV Raymond-Smith thermal component with $0.5 - 2$ keV and $2 - 10$ keV luminosities of $\log L_X = 39.2$ and 39.4 erg s $^{-1}$, respectively, that is coincident with the core radio source in NGC 4552, also consistent with the presence of a weak AGN.

In this work we use *Chandra* X-ray observations to study ram-pressure stripping of gas from the outer regions of NGC 4552, as well as shocks, produced by recent nuclear activity, that are observed close to the galaxy's center. Our discussion is organized as follows: In §2 we describe the observations and our data reduction and processing procedures. In §3 we present the background subtracted, exposure corrected image of NGC 4552 showing all the prominent X-ray emission features of the system: a sharp surface brightness edge to the north, 'horns' of emission extending away to the south from the surface brightness edge, a ram pressure stripped X-ray tail, and bright ring-like features near the galaxy center. We discuss our analysis method and main results, including the determination of the gas density and temper-

ature, for gas stripping from the outer regions of the galaxy. We use these results to constrain the velocity of NGC 4552 through the Virgo ICM. In §4 we focus on the central region of NGC 4552. We model the spectral properties of the rings in the inner 1.3 kpc of the galaxy and use the surface brightness profile to estimate the density jump across the rim of the rings. We show that these rings are consistent with shocked gas driven outward by recent nuclear activity. The spectral properties of the nuclear region are briefly discussed for comparison with earlier work. In §5 we summarize our results. Unless otherwise indicated all errors correspond to 90% confidence levels and coordinates are J2000. Taking the distance to the dominant elliptical M87 as representative of the distance to subcluster A of the Virgo Cluster containing NGC 4552, the luminosity distance to the cluster is 16.1 ± 1.1 Mpc (Tonry et al. 2001) and 1" corresponds to a distance scale of 77 pc.

2. OBSERVATIONS AND DATA REDUCTION

For our analysis, we used a 54.4 ks observation of the elliptical galaxy NGC 4552 in Virgo taken with *Chandra* on 2001 April 22 using the Advanced CCD Imaging Spectrometer array (ACIS, Garmire et al. 1992; Bautz et al. 1998) with ACIS-S (chip S3) at the aimpoint. The focal plane temperature of the instrument was -120° C throughout the observation. The data were analyzed using the standard X-ray processing packages, CIAO version 3.1, FTOOLS and XSPEC version 11.2. Filtering removed events with bad grades (1, 5, and 7) and those with significant flux in border pixels of the 5×5 event islands (VFAINT mode), as well as any events falling on hot pixels. Use of VFAINT mode improves background rejection by as much as a factor of 3 in the S3 chip for soft X-ray energies (~ 0.3 keV) important to this observation. The data were reprocessed and response files created using the most recent gain tables and instrumental corrections. These included correcting for the time-dependent declining efficiency of the ACIS detector due to the buildup of contaminants on the optical filter (Plucinsky et al. 2003), which is important at energies below 1.5 keV, and for the slow secular drift (tgain) of the average

PHA values for photons of fixed energy.² Periods of anomalously high background (flares) were identified and removed from the data, along with periods of anomalously low count rates at the beginning and end of the observation. This resulted in a useful exposure time of 51,856s.

Backgrounds for use in the imaging analyses and spectral measurements of the Virgo Cluster gas were created from the 450ks period D source free dataset (aciss_D_7_bg_evt_271103) appropriate for the date of observation and instrument configuration.³. Identical cleaning, energy and spatial filters were applied to source and background data throughout. We checked the standard normalization of the source free background, set by the ratio of the exposure times, by comparing count rates between the source and background files in the 9.5 – 12 keV energy range, where particle background dominates. We found the standard normalization was 5% too high and renormalized the source free data by a factor of 0.95 to correct for this difference. Point sources were identified in the $8'.4 \times 8'.4$ field of the S3 chip in the 0.3 – 10 keV energy band using a multiscale wavelet decomposition algorithm set with a 5σ detection threshold. The resulting 132 source identifications were excluded from the spectral and surface brightness analyses that follow.

3. RESULTS: RAM PRESSURE STRIPPING OF NGC 4552

In Figure 1 we present the 0.5 – 2 keV *Chandra* image of the diffuse emission in NGC 4552 overlaid with X-ray surface brightness contours showing the X-ray features of interest for our analysis. Point sources were removed from the image and the holes filled with the local average emission level using CIAO tool *dmfilth*. The image was then background subtracted, corrected for telescope vignetting and detector response using exposure maps created with standard CIAO tools. First, two narrow band (0.5 – 1 and 1 – 2 keV) images were background subtracted and exposure corrected using monoenergetic instrument maps of 0.9 and 1.5 keV, respectively. The fluxed narrow band images were then summed and smoothed

²see Vikhlinin et al. in <http://cxc.harvard.edu/contrib/alexey/tgain/tgain.html>

³see <http://cxc.harvard.edu/contrib/maxim/acisbg>

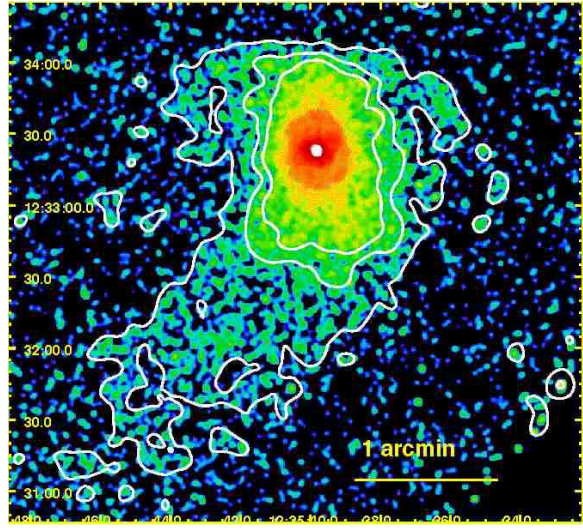


Fig. 1.— *Chandra* image of the 0.5 – 2 keV diffuse emission in NGC 4552 in the Virgo Cluster. Point sources have been removed and the image has been background subtracted, exposure corrected and smoothed with a Gaussian kernel with $\sigma = 1''$. Contours denote X-ray surface brightness levels of $0.4, 1, 2 \times 10^{-8}$ photons $\text{s}^{-1} \text{cm}^{-2} \text{arcsec}^{-2}$, respectively. The X-ray surface brightness exhibits a sharp leading edge $40''$ (3.1 kpc) to the north of the galaxy center, horns of emission extending southeast and southwest of the leading edge, and a $\sim 2'$ (~ 10 kpc) tail of emission to the south-southeast. The bright inner rings of emission $\sim 17''$ (1.3 kpc) from the galaxy’s nucleus are better seen in Figure 6. North is up and east is to the left.

with a $1''$ Gaussian kernel to produce the images in Figure 1. We chose conservative Gaussian smoothing for our images to minimize potential numerical artifacts from the smoothing algorithm. The $1''$ smoothing scale represents a compromise between the need for high spatial resolution to map sharp or narrow features and the need to smooth over larger scales to highlight faint extended emission features. We see a sharp, flattened discontinuity (edge) in the surface brightness 3.1 kpc ($40''$) north of NGC 4552’s center. Horns of emission extend $\sim 3 - 4$ kpc ($\sim 40'' - 50''$) to the southeast and southwest away from each side of the flattened edge. An X-ray tail extends ~ 10 kpc ($\sim 2'$) to the south-southeast before becoming indistinguishable

from the ambient ICM.

Disturbed X-ray morphologies may arise from tidal interactions caused by a recent or ongoing merger, winds of outflowing material due to a recent starburst, or outflows from a central AGN, as well as from ram pressure stripping of the galaxy ISM due to the motion of the galaxy through the ambient Virgo ICM. For NGC 4552 these first three scenarios are disfavored. Tidal (gravitational) interactions act on both stars and gas, producing characteristic stellar tidal streams or tails (Gnedin 2003; Combes 2004). There is no evidence for disturbed morphology in the stellar distribution of NGC 4552 or for significant extragalactic stellar light that might result, if the observed features were of tidal origin.

A second possibility, given the classification of NGC 4552 as a transition nucleus (Ho et al. 1997), is that the distorted X-ray morphology may be due to winds from a compact nuclear starburst. However, the transition nucleus classification for NGC 4552 is weak, due to 30 – 50% uncertainties in the measurement of the $H\beta$ line emission (Ho et al. 1997), and the radio spectrum of NGC 4552 is inconsistent with that expected from such a starburst. The nucleus of NGC 4552 exhibits a compact core radio source with a flat spectrum, whose peak brightness temperature of 7.8×10^8 K (Filho et al. 2004) is several orders of magnitude above the 10^5 K upper limit (Condon et al. 1991) for the brightness temperature of a compact nuclear starburst. In addition, starburst winds tend to produce conical outflows with associated optical line ($H\alpha$) emission from the interaction between the supernova driven ejecta and the surrounding ISM (see, e.g., Strickland et al. 2000 for NGC 253 and Cecil, Bland-Hawthorn & Veilleux 2002 for NGC 3079), which are not seen in NGC 4552.

A third possibility is that AGN outbursts could be responsible for the distorted X-ray morphology seen at large radii in NGC 4552. The nucleus of NGC 4552 does harbor a supermassive black hole (Filho et al. 2004) and does undergo outbursts, as evidenced by the ring structures seen in Figures 1 and 6 and analyzed in detail in §4. However, the X-ray signatures of such outbursts are residual bright-rimmed cavities and buoyant bubbles, as found in M87 (e.g., Forman et al. 2005), and/or X-ray edges corresponding to shocks driven into the ambient medium by the outburst (e.g., Fabian

et al. 2003 for NGC 1275 in Perseus and Nulsen et al. 2004 for Hydra A). This is quite different from the ‘flattened leading edge - trailing tail’ morphology seen in Figure 1.

In contrast, the qualitative correspondence between the main X-ray features shown in Figure 1, i.e. the leading edge, horns, and tail, and those found in simulations (e.g. see Stevens et al. 1999; Toniazzo & Schindler 2001; Acreman et al. 2003) of ram-pressure stripping of elliptical galaxies moving through surrounding cluster gas is striking. However, since none of these simulations model the specific galaxy, orbital, or cluster characteristics of NGC 4552 in Virgo, only a qualitative, not quantitative, comparison of these simulations to our observation should be made. For supersonic stripping, the galaxy ISM is initially pushed back and fanned out (Stevens et al. 1999, Model 1b, Figure 2; Toniazzo & Schindler 2001, Figure 3; Acreman et al. 2003, Figure 2c, $t = 1.6$ Gyr slice) causing the edge between the galaxy gas and the ICM to flatten, as is seen. This sharp surface brightness discontinuity, 3.1 kpc north of the galaxy’s center, coupled with a gas tail in the opposite direction, fixes the galaxy’s direction of motion in the plane of the sky. Irregular filaments of stripped material are also seen in simulation images extending back from the edge, similar to the ‘horns’ we observe in NGC 4552. These filaments signal the onset of Kelvin-Helmholtz instabilities, where stripping is occurring at the boundary between galaxy and ICM gas. In the simulation images, galaxy gas, once stripped and decelerated, forms a distinctive tail of emission behind the galaxy, again similar to what we see in Figure 1. The three dimensional simulations of Toniazzo & Schindler (2001) demonstrate that the tail is in general not axisymmetric with respect to the direction of motion, but may appear angular or curved, as is also found in our image. Thus the most likely explanation for the origin of the features shown in Figure 1 is ram-pressure stripping of galaxy gas due to the motion of NGC 4552 through the Virgo Cluster ICM. In order to investigate quantitatively these complex gas-dynamical processes and test our ram-pressure-stripping hypothesis, we first determine the spectral properties and densities of hot gas in the surrounding ICM and in NGC 4552’s main emission features.

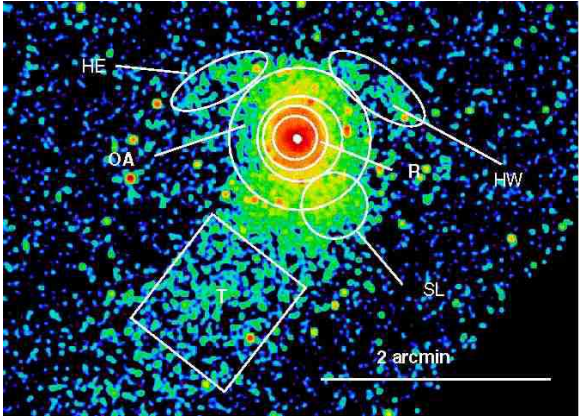


Fig. 2.— Background subtracted, exposure corrected $0.5 - 2$ keV *Chandra* image of NGC 4552 in the Virgo Cluster overlaid with the spectral extraction regions for gas at large radii (OA) in NGC 4552, in the horns (HE, HW), in the southern lump (SL), and in the tail (T), defined in Table 2, and for gas in the inner rings (R) in NGC 4552 (see §4.1). The image has been smoothed with a Gaussian kernel with $\sigma = 1''$.

3.1. Gas Temperatures and Abundances in the Outer Regions

Spectral extraction regions were chosen to isolate, as much as possible given our limited photon statistics, emission from the individual features highlighted in Figure 1. The geometries of these spectral extraction regions are listed in Table 1. In Figure 2 we show the spectral extraction regions used for our analysis. These regions are HE and HW for the eastern and western 'horns' extending from the northern surface brightness edge to either side of the galaxy, OA for galaxy emission at large radii but inside the northern edge, R containing the bright rims of emission discussed in §4, SL a region ('lump') of enhanced emission in the southwestern quadrant of NGC 4552, and T the tail of emission extending from the galaxy to the south. We note that the existence of these features is highly significant with significance levels for HE, HW, R, SL, and T of 106 , 82 , 247 , 6.8 , and 77σ , respectively, relative to that predicted from nearby background regions.

For the analysis below, since the spectra for gas in NGC 4552 and in the X-ray tail are soft, we

restrict the spectral fit energy range for the tail (T), horns (HE+HW) and galaxy regions outside the rings to $0.3 - 2$ keV, where the source count rates are above background. We initially separated the outer annular region (OA) for NGC 4552 into two separate rectangular regions, one just inside the northern leading edge (NG) and one to the south near the beginning of the tail (SG), to look for temperature differences between these two regions. However, since we found no statistically significant difference between the spectral fits for these regions (see Table 2), we combined them into the annular region (OA) shown, in order to improve statistics and sharpen our measurement of the temperature and abundance for galaxy gas outside the central region.

3.1.1. Virgo North (VN) Background Region

We chose a $6'.7 \times 2'.5$ rectangular region (VN) centered $3'$ north of NGC 4552, comprising approximately 25% of the area of the S3 chip, to determine the spectrum of the Virgo Cluster gas in the vicinity of NGC 4552. We fit the spectrum for the Virgo ICM (region VN) over the full $0.3 - 7$ keV energy band, where the S3 detector has good efficiency. We fix the hydrogen absorbing column at $n_{\text{H}} = 2.59 \times 10^{20} \text{ cm}^{-2}$, the Galactic value (Dickey & Lockman 1990) and allow the temperature, abundance and normalization to vary. We find the temperature of the Virgo Cluster ICM to be $2.2_{-0.4}^{+0.6}$ keV with metal abundance $A = 0.1_{-0.1}^{+0.2}$. We then allowed the absorbing column to vary and found no suggestion for increased absorption. Our results are in excellent agreement with previous spectral analyses of the Virgo Cluster ICM using data from *Ginga* (Takano et al. 1989), *ROSAT* (Böhringer et al. 1994), and *ASCA* (Ohashi et al. 1998, Shibata et al. 2001), that find, with Galactic hydrogen absorption, temperatures ~ 2 keV and metal abundances of $\sim 0.1 - 0.3 Z_{\odot}$, at projected distances (~ 300 kpc from M87) comparable to that of NGC 4552. We note that the temperature and X-ray emissivity of the Virgo ICM are relatively insensitive to the metal abundance over the abundance range ($A < 0.3 Z_{\odot}$) determined by our fit. If we allow the abundance to vary over this range, we find variations in the temperature of $\lesssim 0.4$ keV, within the 90% confidence level for the canonical fit, and variations in the inferred $0.5 - 2$ keV X-ray

emissivity for the cluster gas of $\sim 10\%$.

Region VN was also used as a local background region for galaxy source regions at large radii (NG, SG, OA, SL), the horns (HW+HE) and the tail (T), to remove contamination from Virgo Cluster emission. For spectral fitting, counts were grouped both by using predefined bins resulting in channels of approximately logarithmic width, and by using a minimum 20 counts per bin. Both methods gave consistent spectral model fits. The spectra for all of the above regions are well represented by single-temperature APEC or VAPEC thermal plasma models (Smith et al. 2001) corrected for absorption using Wisconsin photo-electric cross-sections (Morrison & McCammon 1983). Our results for these regions are summarized in Table 2.

We checked that our results were not sensitive to the position of the local background region (VN) on the detector by recomputing the spectral fits using a second $100''$ circular region $4''$ east of NGC 4552 (VE in Table 1) and found no significant differences in the fitted parameters. We also fit the spectra to these regions using blank sky backgrounds (as for VN) and a two component APEC + APEC model. We fixed the temperature and abundance of one APEC component at our best fit values for the Virgo Cluster emission ($kT = 2.2$ keV and $A = 0.2 Z_{\odot}$, see Table 2), while allowing the temperature and abundance of the second APEC component and both component normalizations to vary, and found consistent results. Thus our results are not biased by our choice of VN as the local background. Since the models agree within their 90% CL and are simpler when background is subtracted locally, we present only those results (using background region VN) for the tail and galaxy emission at large radii in Table 2.

3.1.2. Outer Annulus (OA) of ISM

For fixed Galactic absorption, we find the temperature and abundance of the outer galaxy gas in region OA to be $kT = 0.43^{+0.02}_{-0.03}$ keV and $A = 0.4^{+0.2}_{-0.1} Z_{\odot}$, a metallicity marginally higher than that for the Virgo ICM, but with large uncertainty. To check the stability of the fit, we allowed the absorbing column to vary and found no suggestion for increased absorption above the Galactic value. To assess the effect of any residual unresolved X-

ray binaries on our results, we also fit the spectrum for region OA, galaxy emission within the northern edge, with an absorbed two component model consisting of an APEC component for emission from the diffuse gas and a 5 keV bremsstrahlung component to model unresolved X-ray binaries (Kraft et al. 2001). We fix the hydrogen absorbing column at its Galactic value, while allowing the temperature and abundance in the APEC component and both component normalizations to vary. We find that unresolved X-ray binaries do not bias our single temperature APEC model results. The bremsstrahlung (unresolved binary) component contributes $\lesssim 5\%$ to the $0.5 - 2$ keV luminosity of region OA, and the fitted temperature ($0.42^{+0.03}_{-0.02}$ keV) and abundance ($0.4^{+0.2}_{-0.1} Z_{\odot}$) for the thermal component are in agreement with the single APEC model results listed in Table 2. The temperature of gas on the galaxy side of the (leading) northern edge is a factor ~ 5 lower than the temperature of the gas in the ambient Virgo ICM. Since, as shown in Figure 1, this temperature drop corresponds to a sharp increase in surface brightness (and thus density as quantified in §3.2), this is consistent with the interpretation of the northern edge as a cold front, the leading edge of the galaxy ISM as it undergoes ram pressure stripping, in broad agreement with expectations from simulations (e.g. see Stevens et al. 1999, Figure 2, model 1b; Acreman et al. 2003, Figures 10a & c and 11b&d, 1.6 Gyr time slice).

3.1.3. Southern ‘Lump’ (SL) Spectrum

Figure 1 also shows a bright region (lump) of emission in the outer southwest quadrant of the galaxy. We use a $17''$ circular region centered at $(\alpha = 12^h35^m38.5^s, \delta = +12^{\circ}32'48''.2)$ surrounding the lump (region SL in Figure 2) to isolate the spectrum for this region. Although we find, using an APEC model with Galactic absorption, a temperature $kT = 0.40^{+0.03}_{-0.02}$ keV and abundance $A > 0.5$ formally consistent with the properties of galaxy gas elsewhere outside the central rings in NGC 4552, the $\chi^2/\text{dof} = 39/26$ is large. The fit is improved ($\chi^2/\text{dof} = 29/26$) by using an absorbed VAPEC model with the iron abundance free to vary while fixing all other abundances at $A = 0.4 Z_{\odot}$, the “best fit” value for galaxy gas at large radii. The hydrogen absorbing column remained fixed at the Galactic value.

We include this fit in Table 2. In this VAPEC model, the temperature of the gas in the southern lump is $kT = 0.38 \pm 0.03$ keV, consistent with previous results for gas at large radii, but the iron abundance is increased to near solar values ($A_{\text{Fe}} = 0.8 \pm 0.2 Z_{\odot}$). This may suggest that the southwest quadrant of the galaxy has either experienced a recent episode of star formation itself or has had metals transported from star forming activity near the galaxy center (expected for a transition type nucleus) to larger radii in the galaxy as a result of outflows.

3.1.4. East and West Horns (HE, HW)

Since the combined region HE+HW for the horns contains only 340 source counts, as shown in Table 2, we only consider simple spectral models (≤ 3 free parameters) for this region. Neither an absorbed bremsstrahlung model nor absorbed power law model, each with all parameters free to vary, can fully describe the data, giving unacceptable reduced χ^2 values of 3.3 and 3.8, respectively. A thermal APEC model with Galactic absorption does provide a reasonable fit to the data with temperature $kT = 0.46^{+0.08}_{-0.07}$ keV and abundance $A = 0.2^{+0.2}_{-0.1} Z_{\odot}$, although the $\chi^2/\text{dof} = 1.7$ is still somewhat large. This most likely reflects a more complex mixture of metal abundances in the horns that could be better addressed using a VAPEC model given a longer exposure and better statistics. As was found for region SL (see Table 2), use of the VAPEC model may marginally decrease the best fit temperature for gas in the horns compared to that found in the simple APEC model fit. In either case, the temperature of gas in the horns is much less than the 2.2 keV temperature of the Virgo ICM, demonstrating that the horns are composed mainly of galaxy gas, likely in the process of being stripped. This is consistent with simulations of ram-pressure stripping (see, e.g. Stevens et al. 1999, Figure 2, model 1b), where the irregular filaments due to the onset of hydrodynamical instabilities during stripping are cooler and denser than the surrounding ICM.

3.2. Gas Densities from Fitting the Surface Brightness Profile

In Figure 3 we show the angular sector used to construct the 0.5 – 2 keV surface brightness

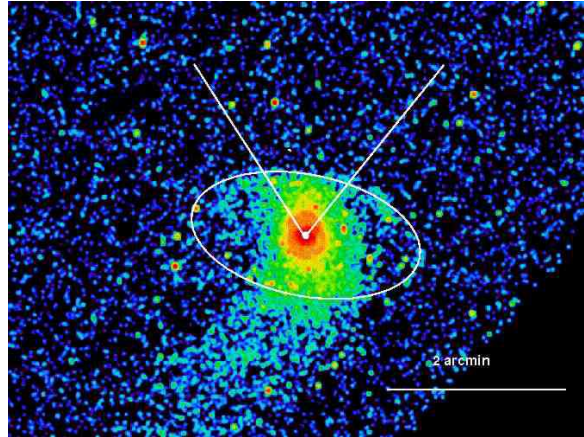


Fig. 3.— Background subtracted, exposure corrected 0.5 – 2 keV *Chandra* image of NGC 4552 in the Virgo Cluster overlaid with the angular sector and bounding ellipse used to extract the surface brightness profile shown in the left panel of Figure 4. The image has been smoothed with a Gaussian kernel with $\sigma = 1''$.

profile to the north across the flattened surface brightness edge between galaxy gas and the Virgo Cluster ICM, as a function of the mean distance from the center of NGC 4552. The profile is constructed from elliptical annuli constrained to lie within the angular sector centered on the galaxy nucleus and extending from 57° to 129° measured clockwise from east, that was chosen to exclude the horns of emission extending southward from each side of the northern leading edge. The elliptical annuli are concentric to a ‘bounding’ ellipse, with semi-major (-minor) axes and position angle of $78''$ ($40''.5$) and 349° , respectively, that traces the shape of the northern surface brightness edge within the angular sector. The radial extent of each elliptical annulus varies logarithmically inward and outward from the bounding ellipse with logarithmic step size 1.1.

In the left panel of Figure 4, we show the 0.5 – 2 keV surface brightness profile as a function of the mean distance from the center of NGC 4552 to the north across the flattened surface brightness edge between galaxy gas and the Virgo Cluster ICM. Two sharp surface brightness discontinuities (denoted by vertical dashed lines) are evident in Figure 4: the outer, ‘leading’ edge is at the north-

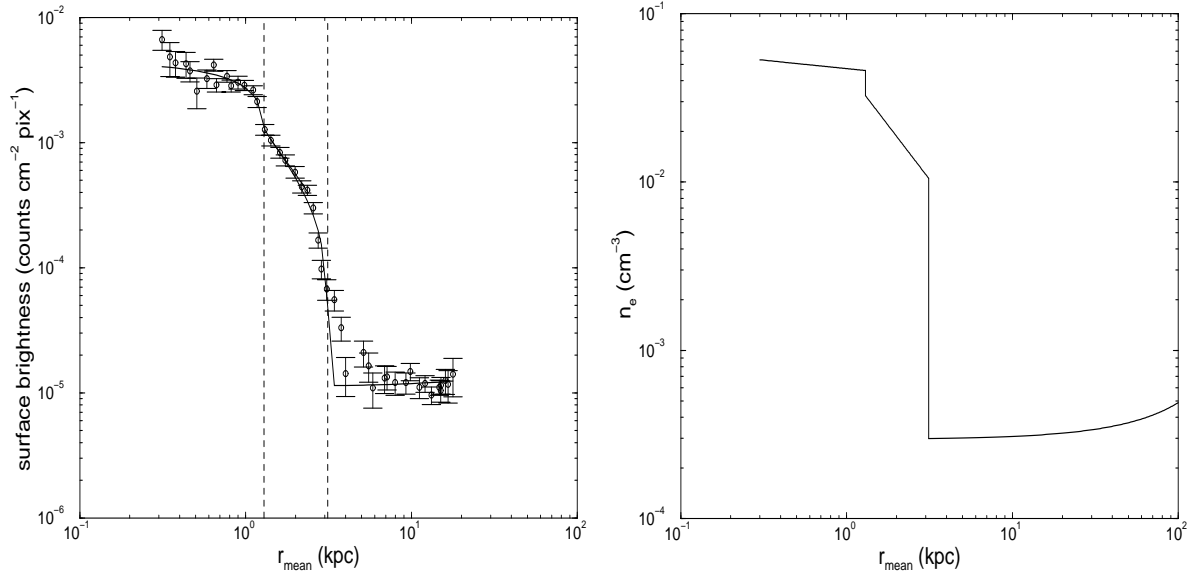


Fig. 4.— (left) The 0.5 – 2 keV surface brightness profile as a function of distance from the center of NGC 4552 toward the north across the galaxy’s leading edge. The vertical dashed lines denote $r_1 = 1.3$ kpc and $r_2 = 3.1$ kpc, the position of the outer radius (rim) of the northern ring and the outer leading edge of the cold front, respectively. The solid line denotes the model results for the surface brightness for power law density models ($n_e \propto r^{-\alpha}$ within the galaxy with $\alpha = 0.1^{+0.25}_{-0.1}$ for $r < 1.3$ kpc (inside the rim) and $\alpha = 1.3^{+0.2}_{-0.2}$ for $1.3 \leq r < 3.1$ kpc (between the rim and the leading edge of the cold front). For $r \geq 3.1$ kpc the Virgo ICM is modeled by a β model with index $\beta = 0.47$ and core radius $r_c = 2'.7$ (Schindler et al. 1999). (right) The electron density as a function of radius from the center of NGC 4552 for the above model.

ern interface between the galaxy cold front and Virgo Cluster gas, and the inner discontinuity is at the position of the rim of the bright northern ring. We analyse the leading edge of the cold front in this section and the central rings in §4.

The observed surface brightness profile is proportional to the product of the X-ray emissivity and the square of the electron density, integrated along the line of sight. By fitting the surface brightness profile, we are able to determine the shape of the density distribution, the location of the edge, and the ratio of electron densities on either side of the edge, averaged over the respective profile bins. If the density is slowly varying over the profile bin, as is the case for a cold front, this measured density ratio is a good measure of the physical density discontinuity across the edge.

As was done for other cold fronts (Markevitch et al. 2000; Vikhlinin et al. 2001; Machacek et al. 2005a), we assume a spherically symmetric

power law distribution of the form

$$n_e = n_{e2} \left(\frac{r}{r_2} \right)^{-\alpha_2} \quad (1)$$

for the electron density in NGC 4552 inside the leading edge of the cold front (but outside the central rings), where n_{e2} and α_2 are the normalization and power law index for the electron density of NGC 4552 in the cold front, respectively. The radial distance r and location r_2 of the leading surface brightness discontinuity are measured from the optical center of NGC 4552, i.e. the center of the bounding ellipse.

We model the electron density in the Virgo Cluster ICM (within subcluster A) using a spherically symmetric, isothermal β model centered on M87 with $\beta = 0.47$, and core radius $r_c = 2'.7$ taken from a fit by Schindler et al. (1999) to *ROSAT* All-Sky Survey data of the Virgo ICM out to a radius of 250' from M87. We normalize the cluster β model using the surface bright-

ness ~ 8 kpc away from NGC 4552, in the undisturbed Virgo ICM (cluster free stream region). We find the central electron density (density β model normalization) for the Virgo ICM to be $n_0 = 0.030 \pm 0.003 \text{ cm}^{-3}$, in agreement with previous results (Schindler et al. 1999).

However, to model the electron density at the interface between galaxy gas in the cold front and the Virgo ICM, requires additional assumptions about the three-dimensional geometry of NGC 4552 relative to the cluster center. We assume that the distance of M87 is representative of the cluster center, at least for subcluster A containing both galaxies. Measurements of distance moduli DM for NGC 4552 ($DM = 30.93 \pm 0.14$) and M87 ($DM = 31.03 \pm 0.16$), using I-band surface brightness fluctuations (Tonry et al. 2001), agree within uncertainties, suggesting the two galaxies are at comparable distances. We thus assume that the 71.6' projected distance between NGC 4552 and M87 is representative of their true physical separation. The electron density of the Virgo ICM at r_2 , just outside the leading edge, is then $n_{ec} = 3.0 \pm 0.3 \times 10^{-4} \text{ cm}^{-3}$.

We then use a multivariate minimization algorithm to fit the surface brightness profile across the leading edge, allowing the location of the edge (r_2), the power law index of the electron density inside the edge (α_2) and the discontinuity (J) to be free parameters. The discontinuity (jump J) is given by

$$J = \left(\frac{\Lambda_{\text{in}} n_{\text{in}}^2}{\Lambda_{\text{out}} n_{\text{out}}^2} \right)^{1/2}, \quad (2)$$

where $\Lambda_{\text{in}}(n_{\text{in}})$ and $\Lambda_{\text{out}}(n_{\text{out}})$ are the X-ray emissivity (electron density) inside ($r \leq r_2$) and outside ($r \geq r_2$) the leading edge of the cold front. We find the best fit position of the leading, northern edge (cold front) to be $r_2 = 3.12^{+0.01}_{-0.02}$ kpc from the galaxy center, the slope of the electron density inside the cold front to be $\alpha_2 = 1.3 \pm 0.2$, and the discontinuity J (given by equation 2) to be 54 ± 4 , where the uncertainties on the discontinuity reflect the 90% CL uncertainties in the slope found for α_2 .

While the surface brightness jump J depends only on the slope of the power law distribution given by the fit to the surface brightness profile, we see from equation 2 that the ratio of the electron densities inside and outside the leading edge

are sensitive, through the X-ray emissivity, to the spectral properties of the gas. In Table 3 we show the dependence of the spectral fit parameters on the galaxy abundances for all the galaxy regions of interest and list the parameters for the nearby Virgo Cluster ICM for comparison. The temperature found for gas in each region is insensitive to the abundance over the range of interest ($\sim 0.3 - 1 Z_{\odot}$). On the other hand, since metal lines dominate the cooling function for temperatures $\lesssim 1 \text{ keV}$ (Tucker & Gould 1966; Raymond & Smith 1977; Smith et al. 2001), the spectral model normalization, and thus X-ray emissivity, vary by more than a factor of 2 over the same range. As shown for NGC 1404 in Fornax (Machacek et al. 2005a), this may introduce significant uncertainties in modeling the electron density in the galaxy from the surface brightness discontinuity between galaxy and cluster gas.

We use $0.5 - 2 \text{ keV}$ X-ray emissivities given in Table 3 derived from our spectral fits, the cluster ICM density outside the cold front ($n_{ec} = 3.0 \times 10^{-4} \text{ cm}^{-3}$) determined from the cluster ICM β -model, and the measured discontinuity (54 ± 4) in equation 2 to infer the electron density n_{e2} inside the cold front. In Table 4 we show the effect of the uncertainty in NGC 4552's abundance (and thus emissivity) on the ratio of electron densities inside and outside the leading edge (cold front) and the propagation of that uncertainty through the analysis of the galaxy motion that follows. However, since we found no strong metallicity gradients within the galaxy, we adopt, for definiteness, a common mean metallicity for gas in the whole galaxy of $A = 0.6 Z_{\odot}$ (see Table 2 and §4.1) and the corresponding $0.5 - 2 \text{ keV}$ emissivity for 0.43 keV galaxy gas at large radii of $\Lambda_{\text{in}} = 1.2 \times 10^{-23} \text{ erg cm}^3 \text{ s}^{-1}$. We take the $0.5 - 2 \text{ keV}$ X-ray emissivity for $A = 0.1 Z_{\odot}$ Virgo ICM gas (from Table 3) to be $\Lambda_{\text{out}} = 5 \times 10^{-24} \text{ erg cm}^3 \text{ s}^{-1}$. The density ratio across the cold front is then found to be $n_{e2}/n_{ec} = 35$, and the electron density at $r_2 = 3.1 \text{ kpc}$, inside NGC 4552 in the cold front, is $n_{e2} = 0.01 \text{ cm}^{-3}$.

3.3. The Leading Edge of the Cold Front: Constraining NGC 4552's Velocity

Following Vikhlinin et al. (2001), we use the temperature and density ratios across the leading edge in NGC 4552 to calculate the pressure ratio

p_2/p_c between galaxy gas in the cold front inside the leading edge and undisturbed Virgo cluster gas in the free-stream region. We assume the galaxy gas in NGC 4552 just inside the edge is in pressure equilibrium with cluster gas at the stagnation point just outside the edge, where the relative velocity between NGC 4552 and the cluster gas is zero. Thus p_2/p_c is a measure of the pressure ratio between cluster gas at the stagnation point and in the free-stream region, and can be used to determine the Mach number M of NGC 4552's motion relative to the ICM (Landau & Lifschitz 1959; Vikhlinin et al. 2001). In Table 4 we summarize the dependencies of this velocity analysis for NGC 4552 on the metallicity of the galaxy gas over the abundance range $0.4 - 1.0 Z_\odot$. It is important to note that, because the motion lies on the supersonic, steeply rising branch of the pressure ratio versus Mach number curve (Eq. 3 in Vikhlinin et al. 2001), the Mach number remains well constrained, despite the large uncertainties in the density and pressure ratios caused by uncertainties in NGC 4552's metallicity.

We find that NGC 4552 is moving at Mach $M = 2.1 \pm 0.2$ through the Virgo Cluster gas. Given the speed of sound in 2.2 keV gas of $c_s = 766 \text{ km s}^{-1}$, the speed of NGC 4552 relative to the ICM is $v = 1610 \pm 150 \text{ km s}^{-1}$. Taking $v_r = -967 \pm 11 \text{ km s}^{-1}$, the relative radial velocity between NGC 4552 and M87 (NED, Smith et al. 2000), as the relative radial velocity between NGC 4552 and the surrounding Virgo ICM, we find the component of velocity in the plane of the sky to be $v_t = 1290^{+180}_{-200} \text{ km s}^{-1}$ and the inclination angle of the motion with respect to the plane of the sky to be $\xi = 37^{+5}_{-4}$ towards the observer.

3.4. The Ram-Pressure Stripped Tail

With the motion of NGC 4552 through the ICM constrained by the properties of the leading cold front, we can examine the properties of the hot gas in the tail. From Table 2, we see that the temperature ($kT = 0.51^{+0.09}_{-0.07} \text{ keV}$) of X-ray-emitting gas in the tail is consistent (given the large uncertainties) with the temperature of gas in region OA ($kT = 0.43^{+0.02}_{-0.03} \text{ keV}$) and in the horns ($kT = 0.46^{+0.08}_{-0.07} \text{ keV}$) of NGC 4552, where stripping is expected to be occurring. The gas temperature in the tail is a factor ~ 4 times lower than that of the Virgo ICM, proving that the tail is composed pre-

dominantly of ram-pressure-stripped galaxy gas rather than Virgo ICM gas concentrated into a wake. Although poorly constrained due to our limited statistics, the metallicity for gas in the tail ($A \sim 0.4^{+2.6}_{-0.2} Z_\odot$) is also consistent with that in the galaxy. The $0.5 - 2 \text{ keV}$ luminosity for hot gas in the tail (from region T) is $\sim 9 \times 10^{38} \text{ erg s}^{-1}$.

We estimate the mean electron density n_{et} for gas in the tail from the XSPEC APEC spectral model normalization K , where

$$K = \frac{10^{-14} n_{\text{et}} n_{\text{Ht}} \eta V}{4\pi (D_A(1+z))^2}. \quad (3)$$

D_A is the angular size distance to the source, z is the source redshift, n_{et} and n_{Ht} are the mean electron and hydrogen number densities, respectively, η is the gas filling factor, and V is the volume of the tail emission region. All quantities are in cgs units. If we assume gas in the tail uniformly fills a cylindrical volume (corresponding to the spectral extraction region T) of radius 2.4 kpc ($31''$) and length $5.3 \text{ kpc} \cos^{-1/2} \xi$, where ξ is the inclination angle of the motion with respect to the plane of the sky, we find a mean electron density for hot gas in the tail of $n_{\text{et}} = 6 \pm 2 \times 10^{-3} \cos^{1/2} \xi \text{ cm}^{-3}$. As shown in Table 3 and reflected by the large uncertainties, the APEC model normalization K , and thus the inferred mean electron density, are strongly dependent on the metallicity of the tail. Assuming the “best fit” model for the trail ($A = 0.4 Z_\odot$, $kT = 0.51 \text{ keV}$, $\xi = 37^\circ$), the mean electron density in the tail (region T) is $5.4 \times 10^{-3} \text{ cm}^{-3}$. Thus the tail is cooler and denser than the surrounding ICM, as expected from simulations (see, e.g. Stevens et al. 1999, Figure 2, Model 1b).

In Figure 5 we compare the surface brightness in a rectangular region of width 5 kpc projected onto the tail's central axis in 1.5 kpc bins along the length of the tail (filled circles) to the projection of the surface brightness of the surrounding Virgo ICM in a parallel region of the same dimensions, orientation, and bin size (open squares). We define the beginning of the tail (and $r = 0$ of the projection in Figure 5) at the point $\sim 4 \text{ kpc}$ south of NGC 4552's center, where the tail visually appears distinct from the galaxy's more spherical, hot gas halo (see Figure 1). The solid and long-dashed lines denote the best linear fits to the projected surface brightness of the tail and Virgo ICM, re-

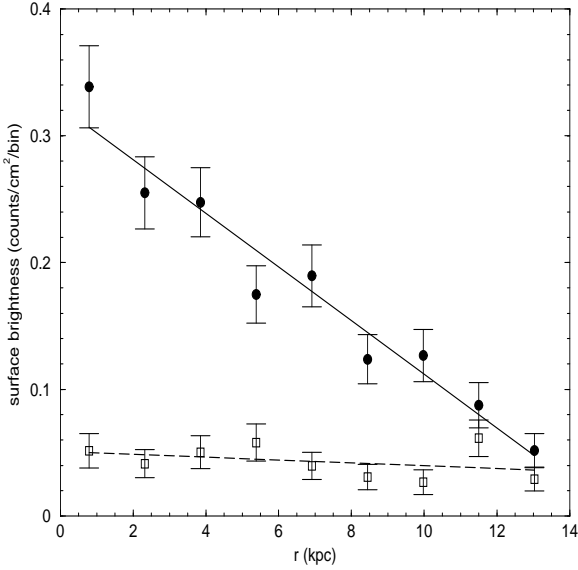


Fig. 5.— Projected surface brightness from the $0.5 - 2$ keV image in Fig. 1 onto the midplane of the tail, measured from 4 kpc south of NGC 4552’s center, where the tail appears to deviate from the hot gas halo of NGC 4552, and summed in 1.5 kpc bins from a rectangular region of width 5 kpc and orientation angle 226° . Open squares represent the projected surface brightness from a parallel region of the same dimensions in the nearby ICM. The solid and dashed lines represent linear regression ($y = ar + b$) fits for the tail and Virgo ICM with slope $a = -0.021 \pm 0.002$ counts $\text{cm}^{-2} \text{bin}^{-1} \text{kpc}^{-1}$ and intercept $b = 0.32 \pm 0.02$ counts $\text{cm}^{-2} \text{bin}^{-1}$ for the tail, and $a = -0.001 \pm 0.001$ counts $\text{cm}^{-2} \text{bin}^{-1} \text{kpc}^{-1}$ and $b = 0.05 \pm 0.01$ counts $\text{cm}^{-2} \text{bin}^{-1}$ for the nearby Virgo ICM.

spectively. As expected from the β -model for the Virgo ICM (Schindler et al. 1999), the projected surface brightness of the Virgo ICM at the distance of the tail from M87 is very flat, consistent with being constant. In contrast the projected surface brightness of the tail declines by a factor ~ 5 before becoming indistinguishable from the surrounding Virgo ICM. Defining the length of the observed tail, in the plane of the sky, as the distance from where the tail appears distinct from NGC 4552 to where it fades into the Virgo ICM, we estimate this length to be ~ 11 kpc (from Fig-

ure 5), corresponding to a physical length (given $\xi = 37^\circ$) of ~ 14 kpc. Using our derived mean density of $\sim 5 \times 10^{-3} \text{ cm}^{-3}$ and assuming uniform filling of a cylindrical volume of radius 2.4 kpc and physical length 14 kpc, we estimate the gas mass in the observed tail to be $M_{\text{tail}} \sim 3 \times 10^7 M_\odot$.

We find the mean thermal pressure for gas in the tail to be $\sim 6 \pm 3 \times 10^{-3} \text{ keV cm}^{-3}$, where the errors reflect the 90% CL combined uncertainties due to the measured tail gas temperature and metallicity and NGC 4552’s inclination angle ξ . We estimate the mean pressure of the surrounding ICM using the Virgo ICM β -model evaluated at the midpoint of the cylindrical emission region (T). Since the perpendicular (ξ dependent) component of the distance between the midpoint of region T and the Virgo Cluster center (taken to be M87) is small ($\sim 0.9' - 1.4'$ for $\xi \sim 30 - 40^\circ$) compared to the transverse component (72'), the ξ dependence of the cluster gas electron density can be ignored. We find the mean thermal pressure for undisturbed Virgo cluster gas at the location of the tail to be $\sim 1.2_{-0.3}^{+0.5} \times 10^{-3} \text{ keV cm}^{-3}$. Although the uncertainties are large, these data suggest that the thermal pressure of the undisturbed ICM alone may not be sufficient to establish pressure equilibrium with the stripped gas in the tail. This is in agreement with simulations that find the stripped ISM may not be in pressure equilibrium with the ambient medium, but that gas in the tail expands while it is removed (Tonizawa & Schindler 2001; Heinz et al. 2003).

If we assume the gas, once heated and stripped from the galaxy, is free to expand adiabatically at approximately the tail sound speed ($c_t \sim 370_{-20}^{+30} \text{ km s}^{-1}$ for $0.51_{-0.06}^{+0.09} \text{ keV}$ gas), we can use the initial tail radius r_{init} to estimate the time t_{eq} needed for gas in the tail to reach pressure equilibrium with the undisturbed ICM (Machacek et al. 2005b), i.e.

$$t_{\text{eq}} = \frac{r_{\text{init}}}{c_t} \left(\frac{p_t}{p_c} \right)^{0.3} \quad (4)$$

for a monatomic ideal gas with adiabatic index $\gamma = 5/3$, where p_t and p_c are the initial and final thermal pressures in the tail. Assuming thermal pressures dominate, the final trail pressure p_c is approximately the pressure of the surrounding ICM. Using the best APEC model fit parameters for the tail gas, $\xi = 37^\circ$, and initial radius

~ 2.4 kpc (from region T), we find the time to expand to equilibrium to be ~ 10 Myr. Given NGC 4552's transverse velocity of ~ 1300 kms, gas at the end of the observable tail (~ 11 kpc downstream in the plane of the sky) has had ~ 8 Myr more time to expand than gas now found near the beginning of the tail, and so the southern end of the tail may be nearly in pressure equilibrium with the ICM.

As the gas density in the tail decreases due to adiabatic expansion, we would expect the tail to broaden and fade. From conservation of entropy, the mean density and temperature of the tail gas at pressure equilibrium would be $n_{\text{eq}} \sim 2 \times 10^{-3} \text{ cm}^{-3}$ and $kT \sim 0.3 \text{ keV}$, with an expected corresponding decrease in surface brightness by a factor ~ 8 . Although our statistics are too limited to directly observe a temperature decline in the tail, the observed rapid fading of the tail, by a factor $\gtrsim 5$ from Figure 5, is broadly consistent with that expected from adiabatic expansion.

3.5. In Search of the Bow Shock

For supersonic motion one would expect a bow shock to form in the Virgo ICM in front of the galaxy. However, the bow shock is likely to be the least visible of the three features (cold front, tail, bow shock) expected from supersonic ram pressure stripping (Stevens et al. 1999). The primary reason for this is that the shock front is narrow and the observed properties are very sensitive to projection effects. While the Rankine-Hugoniot conditions (§ 85 Landau & Lifshitz 1959) predict a peak density and temperature jump of 2.4 and 2.2 at the shock front for Mach 2.1 motion through the cluster gas, the observed temperature and density jumps will be much lower primarily due to integration along the long line of sight that crosses mostly through unshocked cluster gas, and to projection effects caused by the fact that the motion of NGC 4552 is not in the plane of the sky, but at an inclination angle of $\sim 37^\circ$ out of the plane towards the observer.

Following Vikhlinin et al. (2001) we estimate the approximate location of the bow shock in front of the NGC 4552 from the Mach number and the location (x_{sb}, y_{sb}) of the body sonic point, i.e. the point on the body where the flow velocity equals the sound speed of the cluster gas. x_{sb} is the coordinate of the body sonic point measured along

the axis of symmetry and y_{sb} is the radial distance of the body sonic point from the axis of symmetry (see Vikhlinin et al. 2001, Figure 9). As Vikhlinin et al. (2001) describe, we derive the shock position using Moeckel's (1949)⁴ Figure 7, that shows the ratio of the shock detachment distance $L = x_0 - x_{sb}$, where x_0 is the location of the bow shock along the symmetry axis, versus the radial coordinate of the body sonic point y_{sb} as a function of the Mach number. For a Mach 2.1 shock, $L/y_{sb} \approx 0.8$. Thus if the body sonic point is known, the calculation of the shock position is well determined. If the body being stripped has a well defined shoulder, as in A3667 (Vikhlinin et al. 2001), the body sonic point is at the location of the shoulder. However, in NGC 4552 (see Figure 1), the 'horns' make the precise location of the shoulder difficult to discern. Instead we use Figure 9 of Moeckel (1949) to find the body sonic point for Mach 2.1 motion as that point on the body surface where the angle, θ_d , of the tangent line from the symmetry axis to the body surface is $\theta_d \approx 42^\circ$. Again the precise shape of the body surface is uncertain due to the irregular 'horns'. We estimate the 'body surface' of the galaxy by a sphere centered on the galaxy nucleus with a radius of 3.1 kpc (the radial distance to the leading edge). This approximately spherical shape is consistent with the distribution of optical light and broadly consistent with the galaxy gas not in the horns. We then find $y_{sb} \approx 2.5$ kpc, the shock detachment distance $L \approx 2$, and the distance $x_b - x_{sb}$, between the position of the leading edge x_b and the body sonic point along the symmetry axis, of ≈ 1 kpc. Rewriting the shock detachment distance $L = x_0 - x_b + x_b - x_{sb}$, we expect the bow shock to intersect the symmetry axis at ≈ 1 kpc outside the leading edge or equivalently at $r \approx 4$ kpc from NGC 4552's center. It is interesting to note that the surface brightness outside the leading edge, shown in Figure 4, does increase by a factor ~ 2 between $r \sim 4-6$ kpc, broadly consistent with this picture. While suggestive, a much deeper observation is needed to establish whether or not this rise is actually evidence for the expected bow shock.

The density and thus surface brightness are also expected to rise in the stagnation region as the

⁴Approximate Method for Predicting Form and Location of Shock Waves, NACA Technical Note 1921. Available online at <http://naca.larc.nasa.gov/reports/1949/naca-tn-1921>.

gas behind the shock slows and is adiabatically compressed in front of the leading edge (Vikhlinin et al. 2001). Again a rise in the surface brightness is observed in Figure 4 in front of the northern edge ($r \sim 3.1\text{kpc}$). However, this observed rise in surface brightness could also partly be due to galaxy gas being stripped by instabilities to form the horns. The expected temperature rise in the gas behind the shock front, as seen, e.g., in simulation slices by Stevens et al. 1999, would also not be observable in our data due to dilution by unshocked gas projected along the line of sight and our limited statistics over the small region (Mach angle $\sim 28^\circ$) between the shock front and the galaxy.

4. NUCLEAR OUTFLOWS IN NGC 4552

In Figure 6 we show the $0.5 - 2\text{ keV}$ diffuse emission from the two ring-like features in the central region of NGC 4552. The rings are approximately spherical and of equal size with radii $\sim 0.85\text{kpc}$ ($11''$) and farthest projected distance from the nucleus of NGC 4552 of $\sim 1.3\text{kpc}$ ($\sim 17''$), creating in projection the 'hourglass' appearance noted by Filho et al. (2004). Such cavities have been shown in other elliptical galaxies, such as M87 (Forman et al. 2005), to chronicle past episodes of nuclear activity from a central AGN. Whether or not such nuclear activity may be related to ram-pressure stripping remains controversial. Simulations do suggest, however, that, in some cases, ram-pressure may cause counter-streaming of the gas behind the galaxy back onto the galaxy's center (Stevens et al. 1999, Toniazzo & Schindler 2001, Acreman et al. 2003). Such inflows might trigger a starburst, or feed a central black hole causing episodic outbursts (Binney & Tabor 1995). Thus the presence of nuclear activity in galaxies undergoing ram-pressure stripping may be more than coincidental and may be an important factor preventing the order of magnitude increase in galaxy central density found in these simulations.

4.1. Gas Temperature and Density in the Rings

We fit the spectrum of the rings in an annular region R, shown in Figures 2 and 6 and listed in Table 5, with inner and outer radii of $11''$ and $17''$, respectively. The local background region

for the rings (also listed in Table 5) was chosen concentric to and immediately outside the source to remove contamination from galaxy emission at larger radii as well as the Virgo ICM. We use an absorbed APEC thermal plasma model, with the absorbing column fixed at the Galactic value, to fit the resulting 1840 net source counts over the $0.3 - 3\text{ keV}$ energy range, where the source count rate was significantly above background. We again allowed the hydrogen column to vary and found no suggestion for increased absorption above Galactic. We also verified that there were no significant differences between the spectra for the northern and southern rings by fitting the northern and southern halves of region R separately. We found the temperature and abundance of the northern (southern) ring to be $0.64 \pm 0.03\text{ keV}$ ($0.65^{+0.03}_{-0.04}\text{ keV}$) and $0.6^{+0.4}_{-0.3} Z_\odot$ ($> 0.5 Z_\odot$), respectively, for fixed Galactic absorption. Since the spectral fits for the northern and southern rings agreed within errors, we combined these regions into the single annular region R to improve statistics.

The best fit APEC model spectral parameters for gas in the rings from this combined annular region (Region R) are listed in the first row of Table 6. We find the temperature and abundance of gas in the rings to be $kT = 0.64^{+0.03}_{-0.02}\text{ keV}$ and $A = 0.7^{+0.4}_{-0.2} Z_\odot$ ($\chi^2/\text{dof} = 46/55$), respectively. Thus the temperature of gas in the rings (region R) is a factor 1.4 higher than the surrounding 0.43 keV galaxy gas. This is in contrast to the properties of a cold front, where the brighter region is cooler than its less bright surroundings. We verified that the temperature rise in the rings cannot be due to unresolved X-ray binaries in our data by adding a 5 keV bremsstrahlung component to our spectral model, as in §3.1, and refitting the spectrum. The resulting best fit showed the bremsstrahlung (X-ray binary) component contributed $< 4\%$ to the $0.5 - 2\text{ keV}$ luminosity of region R. The best fit temperature ($0.63 + 0.03 - 0.02\text{ keV}$) and abundance ($A = 0.9^{+0.5}_{-0.3} Z_\odot$) for the thermal component in this model were consistent with the single APEC model results. Although the uncertainties are large, the metallicity in the rings is also consistent with that found in the outer regions of the galaxy. Thus we find no evidence for a strong metallicity gradient across the rings. For completeness we list in Table 6 the metallicity depen-

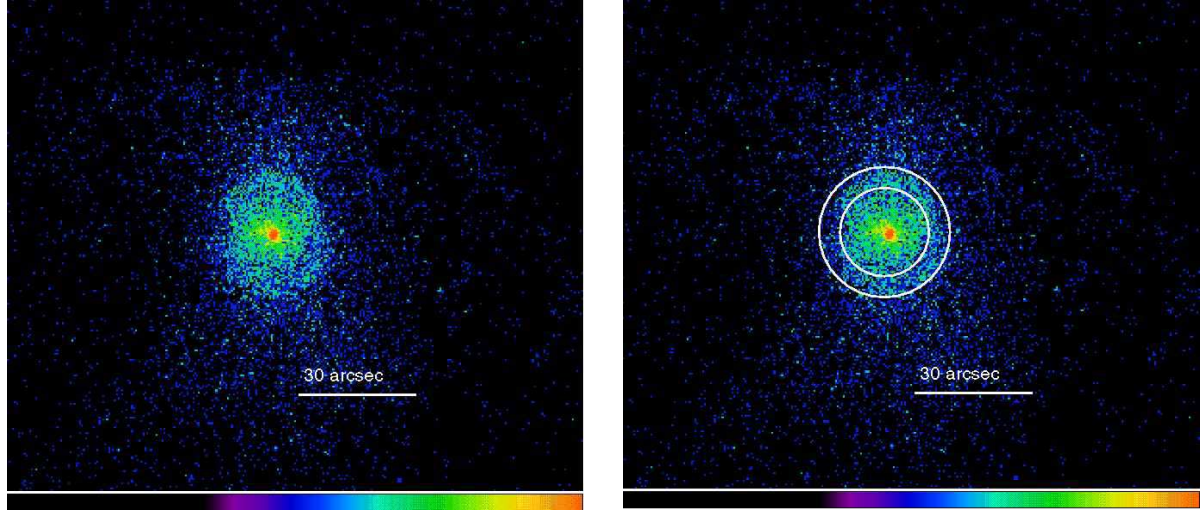


Fig. 6.— (left) Background subtracted *Chandra* image of the 0.5–2 keV diffuse emission from the inner rings in the central region of NGC 4552. (right) The same image with spectral region R superposed. 1 pixel = 0.49 × 0.49.

dence of the 0.5–2 keV X-ray emissivity for gas in the rings over the abundance range (0.4–1.0 Z_{\odot}) of interest for NGC 4552.

As shown in Figure 7, the 0.5–2 keV surface brightness profiles across the northern and southern rims, taken in an angular sector centered on the nucleus extending from 64° to 121° for the northern rim and 257° to 349° for the southern rim (measured clockwise from the +x axis in Figure 6), agree within errors. Thus we use the surface brightness profile across the northern rim as representative of the ring system. We again use the multivariate minimization technique described in §3.2 to determine the electron density inside the rim of the northern ring from the surface brightness profile shown in Figure 4. We assume a spherically symmetric power law distribution for the electron density for $r \leq r_1$, where r_1 is the outer radius (rim) of the ring, of the form

$$n_e = n_{\text{rim}} \left(\frac{r}{r_1} \right)^{-\alpha_1}, \quad (5)$$

where n_{rim} and α_1 are the normalization and power law indices, respectively, for the density of NGC 4552 inside the rim of the northern ring. The density model for NGC 4552's gas outside the ring $r_1 \leq r \leq r_2$ is given in equation 1, where $r_2 = 3.1$ kpc from our analysis of the cold front.

Since the radius of NGC 4552 ($\sim 0'.7$) is much smaller than the projected 71'.6 separation between M87 and NGC 4552, the contribution of the cluster ICM to the surface brightness for radii $r \leq 3.1$ kpc (inside the galaxy) is nearly constant, varying by $\lesssim 2\%$. We subtract this ICM contribution from the surface brightness profile within NGC 4552 ($r < 3.1$ kpc) and fit the remaining galaxy emission, taking the position r_1 of the rim, the galaxy electron density power law indices α_1 , α_2 , and the discontinuity across the rim as free parameters. The discontinuity across the rim is again given by equation 2, where, now, n_{in} and Λ_{in} denote the electron density n_{rim} and emissivity Λ_{rim} inside the rim of the northern ring and n_{out} and Λ_{out} denote the corresponding properties of galaxy gas outside the rim.

We find a best fit position for the inner discontinuity shown in Figure 4 of $r_1 = 1.30$ kpc, coincident with the rim (outer radius) of the northern ring in Figures 1 and 6, and slope $\alpha_1 = 0.1 \pm 0.3$ for the electron density at $r \leq r_1$. The slope of the electron density distribution for radii $r > r_1$ (outside the rings) was $\alpha_2 = 1.3 \pm 0.2$, consistent with our previous fit in §3.3 for the galaxy gas at large radii. Assuming no strong abundance gradients in NGC 4552 and correcting for the 20% difference in the galaxy gas cooling functions, caused by the

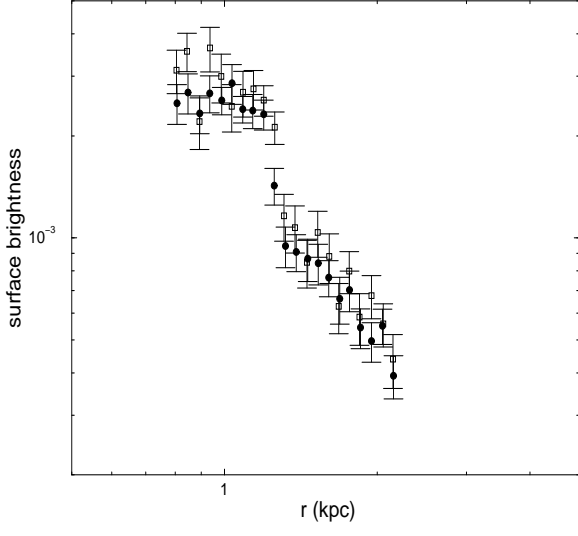


Fig. 7.— The $0.5 - 2$ keV surface brightness profiles across the northern (open squares) and southern (filled circles) rings taken in angular sectors centered on the nucleus extending from 64° to 121° for the northern rim and 257° to 349° for the southern rim (measured clockwise from the $+x$ axis in Figure 6)

difference in gas temperature between gas at large radii (region OA) and gas in the rings (region R), we infer the density ratio across the rim of the northern ring to be $n_{\text{rim}}/n_{\text{out}} = 1.4^{+0.3}_{-0.2}$. Extrapolating equation 1 to $r = 1.3$ kpc, the location of the rim of the northern ring, to evaluate n_{out} at the discontinuity, and using the density discontinuity at the rim, we find the electron density just inside the rim to be $n_{\text{rim}} = 0.05 \text{ cm}^{-3}$. In the right panel of Figure 4, we plot the resulting normalized two power law density model for gas in NGC 4552 and the β -model for the surrounding Virgo ICM as a function of distance from the center of NGC 4552.

4.2. Shocks from Recent Nuclear Activity

Since the temperature ($kT_{\text{rim}} = 0.64$ keV) and density ($n_{\text{rim}} = 0.05 \text{ cm}^{-3}$) of gas in the inner rings are both greater than that for galaxy gas outside the rings ($kT_{\text{out}} \sim 0.43$ keV, $n_{\text{out}} \sim 0.03 \text{ cm}^{-3}$) at $r_1 = 1.3$ kpc, the properties of the rings in Figure 4 are qualitatively consistent with resulting from a shock. For a monatomic ideal gas

with adiabatic index γ , we can use the density discontinuity $\rho_{\text{rim}}/\rho_{\text{out}} = n_{\text{rim}}/n_{\text{out}}$ in the Rankine-Hugoniot shock conditions (Landau & Lifschitz 1959) across the shock to estimate the shock speed (Mach number M_1)

$$\frac{n_{\text{rim}}}{n_{\text{out}}} = \frac{(\gamma + 1)M_1^2}{(\gamma - 1)M_1^2 + 2} \quad (6)$$

and predicted discontinuities in temperature

$$\frac{T_{\text{rim}}}{T_{\text{out}}} = \frac{(2\gamma M_1^2 - (\gamma - 1))((\gamma - 1)M_1^2 + 2)}{(\gamma + 1)^2 M_1^2} \quad (7)$$

and pressure

$$\frac{p_{\text{rim}}}{p_{\text{out}}} = \frac{2\gamma M_1^2}{\gamma + 1} - \frac{\gamma - 1}{\gamma + 1}. \quad (8)$$

We can obtain an estimate for the density jump $n_{\text{rim}}/n_{\text{out}}$ from the surface brightness discontinuity at the position of the rings. However, since the density behind the shock drops sharply due to the rapid adiabatic expansion of the gas, the shock front is narrow. The measured surface brightness discontinuity will underestimate the actual density discontinuity at the shock front, and thus also the inferred shock strength and temperature rise. From our fit to the inner surface brightness edge in §4.1, we inferred a lower limit on the density discontinuity of $1.4^{+0.3}_{-0.2}$. From equation 6 this implies a shock Mach number $M_1 \gtrsim 1.3$. For this Mach number, the temperature and pressure increases predicted by equation 7 and 8 are $T_{\text{rim}}/T_{\text{out}} \gtrsim 1.3$ and $p_{\text{rim}}/p_{\text{out}} \gtrsim 1.8$, in excellent agreement with our measured ratios of $1.48^{+0.15}_{-0.13}$ and $2.1^{+0.7}_{-0.5}$, respectively. Thus the bright rings in Figures 1 and 6 are shocks at the interface between the surrounding galaxy gas and two expanding cavities, like those predicted in numerical simulations to be formed by high-momentum, subrelativistic bipolar nuclear outflows (see e.g. Reynolds et al. 2001; Omma et al. 2004 and references therein).

An estimate for the age of these cavities is given by $t_{\text{age}} \sim R/c_s$ where R is the mean radius of the cavity and c_s is the sound speed in the ambient medium (Birzan et al. 2004). For $R \sim 0.85$ kpc and $c_s \sim 342 \text{ km s}^{-1}$, the speed of sound in 0.43 keV galaxy gas, we find the cavities to be ~ 2.4 Myr old. A lower limit on the total mechanical energy E_{mech} carried in the outflow is given by the work $2p_g V$ needed to evacuate the

two observed cavities, where p_g is the mean pressure of the unshocked galaxy gas at each cavity's center and V is the volume of the cavity. Assuming spherical symmetry for each expanding cavity and extrapolating the density model in equation 1 for unshocked galaxy gas outside the rings to the center of each cavity, we find the sum of the mechanical energy for the two cavities to be $E_{\text{mech}} > 1.2 \times 10^{55}$ erg. This gives a lower limit on the total mechanical power for the outburst of $L_{\text{mech}} > 1.5 \times 10^{41}$ erg s $^{-1}$.

Following Nulsen et al. (2005), we use a simple spherical shock model to obtain a second estimate for the properties of the outflow. Assuming the galaxy gas is in hydrostatic equilibrium, we use our fits to the outer region (OA) of NGC 4552 as representative of the temperature ($kT = 0.43$ keV) and density distribution ($\propto r^{-1.3}$) of the preshocked galaxy gas. We then propagate a non-relativistic spherical shock produced by a point explosion at the center of the galaxy through the surrounding gas and compare the model results to the measured surface brightness profiles for NGC 4552. Although this point explosion model will not reproduce the detailed (bipolar) geometry of the outflows, the model does provide a good description of the shape of the surface brightness profile across the rim and thus a reasonable measure of the Mach number of the shock (Nulsen et al. 2005). In the left panel of Figure 8 we see that the surface brightness profile across the rim of the northern ring in NGC 4552 is well represented by a shock model with Mach number $M_1 = 1.7^{+0.2}_{-0.1}$ and shock radius of 1.29 kpc. The predicted temperature profile across the shock front for the $M_1 = 1.7$ model, uncorrected for projection effects, is shown as the solid line in the right panel of Figure 8. The radial extent of region R ($0.9 \lesssim r \lesssim 1.29$ kpc), used to measure the temperature inside the rings, is much larger than the radial width of the shock. Our measured temperature represents an average over this region. Projection effects also tend to reduce the observed temperature, since any given line of sight through the shock also passes through surrounding unshocked galaxy gas of lower temperature. The dashed line in the right panel shows the predicted emission-measure-weighted temperature profile T_{proj} for our Mach 1.7 model, taking into account the contribution from cooler preshocked galaxy gas along the

line of sight. The emission-measure-weighted temperature profile rises sharply at the shock boundary, peaking at ~ 0.6 keV, and then slowly decreases to ~ 0.55 keV at $r = 0.9$ kpc, the inner radius of region R. This predicted profile is shifted up or down by ~ 0.03 keV due to uncertainties in the temperature of the preshocked galaxy gas. Since the model T_{proj} includes the contribution of unshocked galaxy gas at radii larger than that of the rings, that we subtracted as a local background in our previous fits to region R, we refit the spectrum for the rings in region R, for comparison with the model, using region VN as the local background, which subtracts only the Virgo ICM and particle backgrounds from the data. We find a mean temperature $kT_{\text{proj}} = 0.61 \pm 0.02$ keV and abundance $A = 0.6 \pm 0.15$ ($\chi^2/\text{dof} = 51.8/55$) for fixed Galactic absorption, in excellent agreement with the shock model prediction (Figure 8, just behind the shock). We again checked that this result was not biased by our choice of local background VN by fitting the spectrum (as in §3.1) using blank sky backgrounds and a second APEC component with parameters, other than normalization, fixed at the Virgo Cluster values and found no significant differences.

We now use this shock model to estimate the total mechanical energy and mean mechanical power required for the nuclear outburst. As discussed by Nulsen et al. (2005), these point explosion model estimates of the mechanical energy and mean mechanical power carried in the outburst are likely to be accurate to within about a factor of two. The elapsed time since the nuclear outburst (shock age) in the Mach 1.7 spherical shock model is 1.3 Myr. Since the simplified spherical model geometry overestimates the volume swept out by the observed shocks, the model predictions for the total mechanical energy E_{mech} carried in the shocks and thus also the mean mechanical power L_{mech} of the outburst are upper bounds on the properties of the observed outburst in NGC 4552. We correct for this by including a geometrical factor $f_V \leq 1$, where f_V is approximately the ratio of the volume filled by the observed cavities to that of the spherical model. For a Mach 1.7 shock, we find $E_{\text{mech}} = 2.4 \times 10^{55} f_V$ erg and $L_{\text{mech}} = 5.8 \times 10^{41} f_V$ erg s $^{-1}$. Assuming, as before, the observed cavities are well approximated by two spheres of radius $R = 0.85$ kpc,

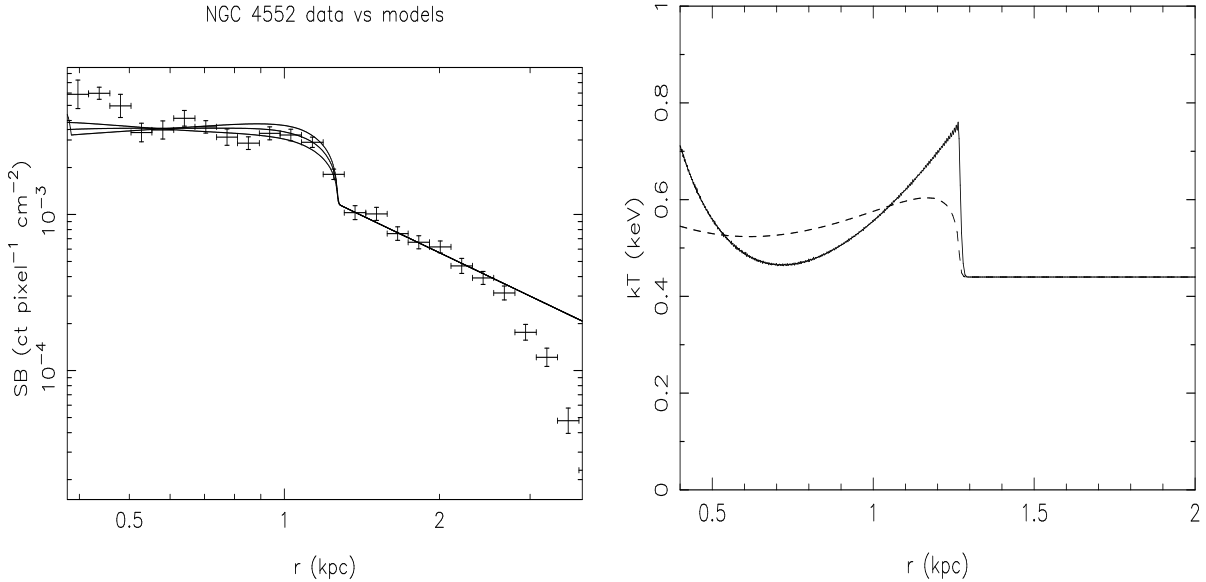


Fig. 8.— (left) Spherical shock model fits to the surface brightness profile across the inner edge for a preshocked isothermal (0.43 keV) $r^{-1.3}$ density distribution inside the galaxy. Upper, middle and lower lines represent shock Mach numbers 1.9, 1.7 and 1.6, respectively. (right) Temperature profile (solid line) for the Mach 1.7 model shock shown in the left panel. Dashed line denotes the emission-measure-weighted temperature profile for lines of sight through the galaxy.

the fraction of the model volume filled by these cavities is $f_V \sim 0.6$, such that the total mechanical energy and mean mechanical luminosity of the outburst are $E_{\text{mech}} \sim 1.4 \times 10^{55}$ erg and $L_{\text{mech}} \sim 3.3 \times 10^{41}$ erg s $^{-1}$, respectively, consistent with our previous estimate.

We obtain an estimate of the total X-ray cooling rate for the galaxy ISM by fitting a mean spectrum for NGC 4552 extracted from a 50'' (3.8 kpc) circular region centered on the galaxy's nucleus, using a two component absorbed APEC model with absorption fixed at Galactic and one set of parameters fixed at the best fit Virgo Cluster parameters. We find a mean temperature (0.57 ± 0.01 keV), abundance ($0.5 \pm 0.1 Z_\odot$), and $0.2 - 2$ keV flux of $F(0.2 - 2) = 7 \times 10^{-13}$ erg s $^{-1}$ cm $^{-2}$ for NGC 4552's ISM component, in excellent agreement with results ($kT = 0.55^{+0.11}_{-0.08}$ keV, $F(0.2 - 2) = 6.8^{+1.1}_{-1.0} \times 10^{-13}$ erg s $^{-1}$ cm $^{-2}$) by Matsushita (2001) using ROSAT data. Using the $0.1 - 14$ keV luminosity as an estimate for the bolometric luminosity L_{bol} of the hot gas, we find $L_{\text{bol}} = 2.5 \times 10^{40}$ erg s $^{-1}$. If we use a more realistic two component temperature model for the ISM, consistent with our spec-

tral results for the individual regions, this estimate of the total flux decreases by $\lesssim 2\%$. Therefore the energy carried in the observed nuclear outflows ($E \sim 1.4 \times 10^{55}$ erg) is sufficient to balance cooling of the galaxy ISM for ≈ 18 Myr.

Using 18 systems, ranging in size from galaxy clusters to the elliptical galaxy M84, containing well defined X-ray surface brightness depressions (cavities), Birzan et al. (2004) found a correlation

$$L_{\text{mech}} = 10^{25 \pm 3} (L_{\text{radio}})^{0.44 \pm 0.06}, \quad (9)$$

albeit with large scatter, between the mechanical power L_{mech} needed to create the X-ray cavities and the total radio power L_{radio} , defined as the integrated radio flux over the 10 to 5000 MHz frequency band, of the source. The error bars of equation 9 denote the extreme values found in their sample. VLBA measurements (Nagar et al. 2002) show that NGC 4552 has a core radio source with two-sided east-west extended emission on ~ 5 milli-arcsecond scales. The radio spectrum is flat, spectral index ~ 0 (Filho et al. 2004), with radio flux densities of 102.1 and 99.5 mJy at 8.4 and 5 GHz, respectively. Follow-

ing Birzan et al. (2004), we find $L_{\text{radio}} = 1.55 \times 10^{38} \text{ erg s}^{-1}$, and from the central values of equation 9, we predict a mechanical power $L_{\text{mech}} \sim 6.4 \times 10^{41} \text{ erg s}^{-1}$, nearly twice that of our estimate. However, given the large scatter in equation 9, our observed value ($L_{\text{mech}} \sim 3.3 \times 10^{41} \text{ erg s}^{-1}$), even with its factor ~ 2 uncertainty, is consistent with this observed correlation. Filho et al. (2004) also argue that the properties of NGC 4552's radio spectrum are most consistent with emission from accretion onto a $\sim 4 \times 10^8 M_{\odot}$ black hole plus a self-absorbed compact jet or outflow. Our observation of shocks produced by outflows from a previous episode of nuclear activity supports this model.

4.3. The Nuclear Region

Finally, we look briefly at the X-ray properties of the nuclear region by modeling the spectrum from a $1''.3$ circular region (NS) centered at ($\alpha = 12^h 35^m 39.8^s$, $\delta = +12^\circ 33' 22.9''$) containing the nuclear source (see Table 5). After local background subtraction using a concentric annular region with inner and outer radii of $1''.6$ and $3''.2$, respectively, the spectrum contains 1046 net source counts in the $0.3 - 5$ keV energy band. An acceptable fit to the data ($\chi^2/\text{dof} = 52/45$) is found using a moderately absorbed ($n_H = 1.1 \pm 0.4 \times 10^{21} \text{ cm}^{-2}$) power law model with steep ($\Gamma = 2.2 \pm 0.2$) photon index. However, adding a second, thermal APEC component to the model improves the fit (see Table 7). For these two component models we first fix the absorbing column at the Galactic value, $n_H = 2.59 \times 10^{20} \text{ cm}^{-2}$, and allow the temperature, metal abundance and photon index to vary, but find the abundance is poorly constrained. We then fix the metal abundance at $A = 0.7 Z_{\odot}$ from the best fit spectral model for the ring region R of NGC 4552 (see the first line in Table 6), and find the fit is unchanged, although the errors on the photon index are modestly reduced. We check the stability of this two component fit by allowing the absorbing column to vary and find n_H consistent with the Galactic value.

In the two component model, we find a photon index $\Gamma \sim 1.7 \pm 0.1$ and temperature $kT = 1.04_{-0.17}^{+0.21} \text{ keV}$. The power law photon index is consistent with those expected for low luminosity AGNs (Terashima & Wilson 2003; Filho et al. 2004). We find intrinsic total $0.5 - 2$ and

$2 - 10$ keV X-ray fluxes in this model to be $5.1 \times 10^{-14} \text{ erg s}^{-1} \text{ cm}^{-2}$ and $6.7 \times 10^{-14} \text{ erg s}^{-1} \text{ cm}^{-2}$, corresponding to $0.5 - 2.0$ keV and $2 - 10$ keV luminosities of $1.6 \times 10^{39} \text{ erg s}^{-1}$ and $2.1 \times 10^{39} \text{ erg s}^{-1}$. The power law component dominates the emission in both energy bands, contributing 75% and 97% of the emission in the $0.5 - 2$ and $2 - 10$ keV bandpasses, respectively. These results are in good agreement with the spectral results of Filho et al. (2004) for a circular region $2''.5$ in diameter surrounding the nucleus with data extracted from the same *Chandra* observation (Obsid 2072) used in this work.

Since the nuclear source is known to be variable at the $\sim 20\%$ level for the 2 and 3.6 cm radio flux on timescales ~ 1 yr (Nagar et al. 2002), it is interesting to look for variability in our X-ray signal. We examined the light curve for a $2''$ circular region centered on the nucleus ($\alpha = 12^h 35^m 39.8^s$, $\delta = +12^\circ 33' 22.9''$) using 3 ks binning and found that the nuclear count rate varied by $\lesssim 2\sigma$ over the 52 ks duration of this observation. However, a regression analysis of these data showed the count rate to be gradually increasing. This was confirmed using an application of the Gregory-Loredo algorithm (1992) on the events time series that showed the variability to be highly significant (Log(OddsRatio) = 36.9) with the normalized odds ratio of 0.95 for the minimum ($m = 2$) binning, consistent with a gradually increasing signal over the duration of the observation.

5. CONCLUSIONS

In this work we analysed a 54.4 ks *Chandra* observation of the elliptical galaxy NGC 4552 in the Virgo Cluster and found X-ray evidence for both ram-pressure stripping in the outer regions of the galaxy, due to its supersonic motion through the Virgo ICM, and for shocks in the inner region of the galaxy from a recent nuclear outburst. We find the following:

1. The $0.5 - 2$ keV X-ray emission shows the classic features of a cold front and ram-pressure stripping as a gas rich galaxy moves supersonically within a rich cluster. We see: (1) a sharp, flattened leading surface brightness edge located 3.1 kpc from the center of NGC 4552 due to the ram-pressure of the Virgo ICM, (2) two horns of emis-

sion extending $3 - 4$ kpc to either side of the edge that are composed of galaxy gas in the process of being stripped due to the onset of Kelvin-Helmholtz instabilities, and (3) a tail of emission extending ~ 10 kpc behind NGC 4552 opposite the leading edge.

2. As expected for a cold front, galaxy gas inside the leading edge is cool ($kT = 0.43$ keV) compared to the surrounding 2.2 keV Virgo ICM. The surface brightness distribution inside the leading edge is well fit by a power law density distribution $n_2 = 0.01(r/r_2)^{-1.3}$ cm $^{-3}$ (for $A \sim 0.6 Z_\odot$), where $r_2 = 3.1$ kpc is the position of the edge. The density ratio between gas inside the cold front and the surrounding Virgo ICM, found from fitting the surface brightness profile, is $n_{e2}/n_{ec} = 35 \pm 7$.
3. Assuming NGC 4552 and M87 both lie in the plane of the sky, the resulting pressure ratio ($\sim 7 \pm 1.4$) between the free-streaming ICM and cluster gas at the stagnation point implies that NGC 4552 is moving supersonically (Mach 2.1 ± 0.2) through the cluster gas with speed $v \sim 1610 \pm 150$ km s $^{-1}$ at an angle $\xi \sim 37^{\circ+5}_{-4}$ towards us with respect to the plane of the sky.
4. The properties of the X-ray tail behind NGC 4552 are consistent with it being composed primarily of ram-pressure stripped galaxy gas. The tail is cool, with mean temperature $kT = 0.51^{+0.09}_{-0.06}$ keV, and denser than the Virgo ICM, with $n_{et} \sim 5.4 \times 10^{-3}$ cm $^{-3}$ for $\xi \sim 37^\circ$. Although the errors are large, mostly due to uncertainties in the tail gas metallicity, the mean thermal pressure of gas in the tail suggests that it is over-pressured with respect to the ambient ICM. The subsequent adiabatic expansion of gas in the tail may partially explain the rapid fading of the tail with distance from the galaxy.
5. Two ring-like emission features, consistent with bipolar nuclear outflow cavities, are found in the X-ray images at $r \sim 1.3$ kpc from NGC 4552's center. The emission measure weighted gas temperature through the rings ($kT_{proj} \sim 0.61 \pm 0.02$ keV) and the shape of the surface brightness profile across the rim of the northern ring are consistent with a simple spherical model for a Mach 1.7 shock from a 1.4×10^{55} erg nuclear outburst $\sim 1 - 2$ Myr ago. The mechanical power carried in the shock, $L_{mech} \sim 3.3 \times 10^{41}$ erg s $^{-1}$, is consistent with that expected from the L_{mech} - L_{radio} correlation (Birzan et al. 2004) between the mechanical luminosity and total radio power for X-ray sources showing nuclear outflow activity. One outburst of this magnitude every ≈ 18 Myr could balance the radiative cooling of NGC 4552's hot ISM.

This work is supported in part by NASA grant GO3-4176A and the Smithsonian Institution. This work has made use of the NASA/IPAC Extragalactic Database (NED) which is operated by the Jet Propulsion Laboratory, California Institute of Technology, under contract with the National Aeronautics and Space Administration. We wish to thank Maxim Markevitch for the use of his edge analysis codes and Arnold Rots for help in analysing the nuclear point source variability.

REFERENCES

Acreman, D., Stevens, I., Ponman, T., & Sakelliou, I. 2003, MNRAS, 341, 1333

Bautz, M.W., et al. 1998, X-ray Optics, Instruments and Missions, ed. R.B. Hoover & A.B. Walker, Proc. SPIE, 3444, 210

Biller, B.A., Jones, C., Forman, W.R., Kraft, R. & Ensslin, T. 2004, ApJ, 613, 238

Binney, J. & Tabor, G. 1995, MNRAS, 276, 663

Birzan, L., Rafferty, D. A., McNamara, B.R., Wise, M.W., & Nulsen, P.E.J. 2004, ApJ, 607, 800

Böhringer, H., Briel, U. G., Schwarz, R. A., Voges, W., Hartner, G., & Trümper, J. 1994, Nature, 368, 828

Brown, B. & Bregman, J. 2000, ApJ, 539, 592

Brüggen, M. & Kaiser, C. R. 2002, Nature, 418, 301

Byrd, G. & Valtonen, M. 1990, ApJ, 350, 89

Canizares, C., Fabbiano, G. & Trinchieri, G. 1987, ApJ, 312, 503

Cecil, G., Bland-Hawthorn, J. & Veilleux, S. 2002, ApJ, 576, 745

Churazov, E., Brüggen, M., Kaiser, C.R., Böhringer, H., & Forman, W.R. 2001, ApJ, 554, 261

Combes, F. 2004, in IAU Symposium 217: Recycling Intergalactic and Interstellar Matter, ed. P.-A. Duc, J.Braine, & E. Brinks, ASP Conference Series, vol. 217 (San Franscisco, Astronomical Society of the Pacific), 440

Condon, J., Huang, Z.-P., Yin, Q.F., Thuan, T.X. 1991, ApJ, 378, 65

Davis, D & White, R. 1996, ApJ, 470, L35

Dickey, J.M. & Lockman, F.J., 1990, ARAA, 28, 215

Dosaj, A., Forman, C., Forman, W.R., Markevitch, M., & Vikhlinin, A. 2002, BAAS, 34, 712

Eskridge, P., Fabbiano, G. & Kim, D.-W. 1995, ApJS, 97, 141

Fabian, A.C., Sanders, J.S., Allen, S.W., Crawford, C.S., Iwasawa, K., Johnstone, R.M., Schmidt, R.W., & Taylor, G.B. 2003, MNRAS, 344, L43

Ferrarese, L. & Merritt, D. 2000, ApJ, 539, L9

Filho, M.E., Barthel, P.D. & Ho, L.C 2000, ApJS, 129, 93

Filho, M.E., Fraternali, F., Markoff, S., Nagar, N.M., Barthel, P.D., Ho, L.D., and Yuan, F. 2004, A & A, 418, 429

Forman, W., Jones, C. & Tucker, W. 1985, ApJ, 293, 102

Forman, W., Schwarz, J., Jones, C., Liller, W.,& Fabian, A. 1979, ApJ, 234, L27

Forman, W., Nulsen, P., Heinz, S., Owen, F., Eilek, J., Vikhlinin, A., Markevitch, M., Kraft, R., Churazov, E., Jones, C. 2005, ApJ, in press, eprint astro-ph/0312576

Garmire, G.P. et al. 1992, AIAA, Space Programs and Technologies Conference, March 24-27, 1992 (Paper 92-1473; New York: AIAA)

Gnedin, O.J. 2003, ApJ, 582, 141

Gregory, P.C. & Loredo, T.J. 1992, ApJ, 398, 146

Gunn, J., & Gott, J. 1972, ApJ, 176, 1

Heinz, S., Churazov, E., Forman, W., Jones, C., & Briel, U.G. (2003), MNRAS, 346, 13

Heinz, S., Reynolds, C, & Begelman, M. 1998, ApJ, 501, 126

Ho, L.C., Filippenko, A.V. & Sargent, W.L.W. 1997, ApJS, 112, 315

Irwin, J.A. & Sarazin, C.L. 1996, ApJ, 471, 683

Kenney, J., et al. 1995, ApJ, 438, 135

Kenney, J., van Gorkom, J.H. & Vollmer, B. 2004, astro-ph/0403103

Kim, D.-W., Fabbiano, G., & Trinchieri, G. 1992, ApJS, 80, 531

Kraft, R., Kregenow, J.M., Forman, W.R., Jones, C., & Murray, S.S. 2005, ApJ, 560, 675

Landau, L.D. & Lifshitz, E.M. 1959, Fluid Mechanics (London: Pergamon), Chapter IX

Lavery, R. & Henry, J.P. 1988, ApJ, 330, 596

Machacek, M., Dosaj, A., Forman, W., Jones, C., Markevitch, M., Vikhlinin, A., Warmflash, A., & Kraft, R. 2005a, ApJ, 621, 663

Machacek, M., Nulsen, P., Stirbat, L., Jones, C. & Forman, W.R. 2005b, ApJ, 630, 280

Markevitch, M. et al. 2000, ApJ, 541, 542

Matsushita, K 2001, ApJ, 547, 693

Matsushita, K., Ohashi, T. & Makishima, K. 2000, PASJ, 52, 685

Mazzotta, P., Markevitch, M., Vikhlinin, A., Forman, W.R., David, L. & VanSpeybroeck, L. 2001, ApJ, 555, 205

Merrifield, M.R. 1998, MNRAS, 294, 347

Moore, B., Katz, N., Lake, G., Dressler, A., & Oemler, A. 1996, Nature, 379, 613

Morrison, R. & McCammon, D. 1983, ApJ, 270, 119

Müller, M., Mair, G., & Hillebrandt, W. 1989, A&A, 216, 19

Nagar, N.M., Falcke, H., Wilson, A.S., & Ulvestad, J.S. 2002, A & A, 392, 53

Nulsen, P.E.J. 1982, MNRAS, 198, 1007

Nulsen, P.E.J., McNamara, B.R., Wise, M.W., & David, L.P. 2005, ApJ, 628, 629

Omma, H., Binney, J., Bryan, G. & Slyz, A. 2004, MNRAS, 348, 1105

Ohashi, T. et al. in IAU symposium 188, The Hot Universe, ed. K Koyama, S. Kitamoto, & M. Itoh (Dordrecht:Kluwer), 317

O'Sullivan, E., Forbes, D.A. & Ponman, T. J. 2001, MNRAS, 328, 461

Plucinsky, P.P., Schulz, N.S., Marshall, H.L., Grant, C.E., Chartas, G., Sanwal, D., Teter, M., Vikhlinin, A.A., Edgar, R.J., Wise, M.W., Allen, G.E., Vi-rani, S.N., DePasquale, J.M. & Raley, M.T. 2003, in Proceedings of The SPIE X-ray and Gamma-Ray Telescopes and Instruments for Astronomy, ed. J.E. Truemper & H. Tannenbaum, Proceedings of The SPIE, 4851, 89

Prigozhin, G., Kissel, S., Bautz, M., Grant, C., LaMarr, B., Forster, R., Richer, G., & Gamire, G. 2000, Proc. SPIE, 4012, 720

Quilis, V., Bower, R.G.,& Balogh, M. L. 2001, MNRAS, 328, 1091

Quilis, V., Moore, B., & Bower, R. 2000, *Science*, 288, 1617

Rangarajan, F.V.N., Fabian, A.C., Forman, W.R., & Jones, C. 1995, *ApJ*, 482, 143

Raymond, J.C. & Smith, B.W. 1977, *ApJS*, 35, 419

Reynolds, C., Heinz, S. & Begelman, M. 2001, *ApJ*, 549, L179

Roberts, M., Hogg, D., Bregman, J., Forman, W.R. & Jones, C. 1991, *ApJS*, 75, 751

Sakelliou, I., Merrifield, M.R., & McHardy, I.M. 1996, *MNRAS*, 283, 673

Scharf, C.A., Zurek, D.R., & Bureau, M. 2004, preprint astro-ph/0406216

Schindler, S., Binggeli, B., Böhringer, H. 1999, *A & A*, 343, 420

Shibata, R., Matsushita, K., Yamasaki, N.Y., Ohashi, T., Ishida, M., Kikuchi, K., Böhringer, H., & Matsumoto, H. 2001, *ApJ*, 549, 228

Smith, R.J., Lucey, J.R., Hudson, M.J., Schlegel, D.J. & Davies, R.L. 2000, *MNRAS*, 313, 469

Smith, R.K., Brickhouse, N.S., Liedahl, D. A. & Raymond, J.D. 2001, *ApJ*, 556, L91

Stevens, I.R., Acreman, D. & Ponman, T.J. 1999, *MNRAS*, 310, 663

Strickland, D., Heckman, T., Weaver, K., & Dahlem, M. 2000, *AJ*, 120, 2965

Sun, M. & Vikhlinin, A. 2005, *ApJ*, 621, 718

Sun, M., Jerius, D. & Jones, C. 2005, *ApJ*, submitted, eprint astroph/0501501

Takano, S. et al. , 1989, *Nature*, 340, 289

Terashima, Y. & Wilson, A. S. 2003, *ApJ*, 583, 145

Tonizzzo, T., & Schindler, S. 2001, *MNRAS*, 325, 509

Tonry, J.L., Dressler, A., Blakeslee, J.P., Ajhar, E.A., Fletcher, A.B., Luppino, G.A. Metzger, M.R. & Moore, C.B. 2001, *ApJ*, 546, 681

Tucker, W. & Gould, R. 1966, *ApJ*, 144, 244

Vikhlinin, A., Markevitch, M. & Murray, S.S. 2001, *ApJ*, 551, 160

Vollmer, B. 2003, *A&A*, 398, 525

Wang, Q.D., Owen, F., Ledlow, M., & Keel, W. 2004, in Proc. IAU Colloq. 195, *Outskirts of Galaxy Clusters: Intense Life in the Suburbs*, ed. A. Diaferio (Cambridge: Cambridge Univ. Press), 78

White, D., Fabian, A., Forman, W., Jones, C. & Stern, C. 1991, *ApJ*, 375, 35

TABLE 1
SPECTRAL ANALYSIS REGIONS OUTSIDE THE CENTRAL 1.3 KPC OF NGC 4552

Region	Shape	Center RA, DEC	Dimensions arcsec	Orientation degrees
VN	rectangular	12 35 37.7, 12 36 16.5	400,150	319
VE	circular	12 35 55.5, 12 34 33.7	100	
NG	rectangular	12 35 39.8, 12 33 53.6	13, 42	0
SG	rectangular	12 35 39.8, 12 32 52.9	19, 65	0
OA	annular	12 35 39.7, 12 33 22.9	22, 37	
SL	circular	12 35 38.5, 12 32 48.2	17	
HW	elliptical	12 35 37.0, 12 33 48.9	30, 12	324
HE	elliptical	12 35 42.6, 12 33 52.9	28, 10	27
T	rectangular	12 35 42.6, 12 31 57.6	69, 62	52

NOTE.—WCS Coordinates for the centers of the regions are J2000. Dimensions specified are radii for circular regions, (inner, outer) radii for annular regions, (length,width) for rectangular regions and semi-(major, minor) axis for elliptical regions. Orientation angles are for the region's major (long) axis measured counterclockwise from west (+x axis in Figure 2). Source regions are also shown in Figure 2 except for regions NG and SG, that were combined into the larger region OA to improve statistics. HW and HE were combined into a single region (HE+HW) in the spectral analysis to improve statistics for the horns.

TABLE 2

BEST APEC MODEL SPECTRAL FITS FOR REGIONS OUTSIDE THE CENTRAL 1.3 KPC OF NGC 4552

Region	Source counts	kT keV	A Z_{\odot}	χ^2/dof
VN	2113	$2.2_{-0.4}^{+0.6}$	$0.1_{-0.1}^{+0.2}$	109/103
NG	456	0.46 ± 0.05	$0.2_{-0.1}^{+0.2}$	14.2/16
SG	1067	0.41 ± 0.03	$0.5_{-0.2}^{+1.0}$	31/35
OA	1982	$0.43_{-0.03}^{+0.02}$	$0.4_{-0.1}^{+0.2}$	52/52
SL	734	$0.40_{-0.02}^{+0.03}$	> 0.5	39/26
SL [†]	734	0.38 ± 0.03	0.8 ± 0.2	28/26
HE+HW	340	$0.46_{-0.07}^{+0.08}$	$0.2_{-0.1}^{+0.2}$	26/15
HE+HW	340	$0.46_{-0.07}^{+0.08}$	0.4^f	30/16
T	504	$0.51_{-0.07}^{+0.09}$	$0.4_{-0.2}^{+2.6}$	14.7/10
T	504	$0.51_{-0.06}^{+0.09}$	0.4^f	14.8/11

NOTE.—Column 2 lists the background subtracted source counts in the $0.3 - 7$ keV energy band for region VN and in the $0.3 - 2$ keV band for regions NG, SG, OA, SL, HE+HW, T. Superscript *f* denotes a fixed parameter. [†] VAPEC model with all abundances other than Fe fixed at $0.4Z_{\odot}$ and A_{Fe} shown. Absorption is fixed at the Galactic value ($n_{\text{H}} = 2.59 \times 10^{20} \text{ cm}^{-2}$) in each region. Errors correspond to 90% confidence limits.

TABLE 3
METALLICITY DEPENDENCE OF GAS OUTSIDE THE RINGS

Region	A Z_{\odot}	kT keV	K 10^{-5} cgs	Λ 10^{-23} erg cm 3 s $^{-1}$	χ^2/dof
VN					
	0.1	$2.2_{-0.4}^{+0.6}$	20.3	0.52	109/104
	0.3	$2.6_{-0.4}^{+0.5}$	17.8	0.58	111/104
OA					
	0.4	0.43 ± 0.02	12.4	0.9	52/53
	0.6	0.42 ± 0.02	8.9	1.2	55/53
	0.8	$0.41_{-0.01}^{+0.02}$	6.9	1.6	59/53
	1.0	0.41 ± 0.02	5.6	1.9	62/53
T					
	0.2	0.53 ± 0.07	4.7	0.6	19.7/11
	0.4	$0.51_{-0.06}^{+0.09}$	2.9	1.0	14.8/11
	0.6	$0.50_{-0.06}^{+0.1}$	2.1	1.4	14.7/11
	0.8	$0.49_{-0.05}^{+0.1}$	1.6	1.8	15.1/11
	1.0	$0.49_{-0.06}^{+0.1}$	1.3	2.2	15.5/11
HE+HW					
	0.2	0.46 ± 0.07	3.4	0.5	26.1/16
	0.3	0.45 ± 0.07	2.5	0.7	27.8/16
	0.4	0.45 ± 0.07	1.9	0.9	29.6/16

NOTE.—Dependence of the model temperature kT , APEC model normalization K , and $0.5 - 2$ keV X-ray emissivity Λ on metal abundance A for the nearby Virgo ICM, for gas in NGC 4552 outside the rings ($r > 1.3$ kpc) and gas in the horns and tail. The regions are defined in Table 1 and best-fit model results listed in Table 2. The abundance (column 2) and hydrogen absorption ($n_{\text{H}} = 2.59 \times 10^{20}$ cm $^{-2}$) are fixed, while the temperature and APEC model normalization are allowed to vary. Errors are 90% confidence limits. “cgs” denotes cgs units for the APEC model normalization as given by XSPEC.

TABLE 4
DERIVED VELOCITIES AND EDGE PROPERTIES FOR DIFFERENT GALAXY ABUNDANCES

A Z_{\odot}	n_{e2}/n_{ec}	T_2/T_c	p_2/p_c	M	v km s^{-1}	v_t km s^{-1}	ξ degrees
0.4	42	0.2	8.4	2.3	1760	1470	33
0.6	35	0.2	7.0	2.1	1610	1290	37
0.8	31	0.2	6.2	2.0	1530	1190	39
1.0	28	0.2	5.6	1.9	1460	1090	42

NOTE.— n_e , T , and p denote the electron density, temperature and pressure in each region specified by subscripts 2 and c for galaxy gas just inside the leading edge of the cold front and cluster gas in the free stream region, respectively (See Vikhlinin et al. 2001). M is the Mach number, v is the total velocity, v_t is the component of velocity in the plane of the sky, and ξ is the inclination angle of motion towards the observer with respect to the plane of the sky, respectively, for NGC 4552 relative to the Virgo ICM, assuming a relative radial velocity between NGC 4552 and the Virgo Cluster (M87) of $v_r = -967 \pm 11 \text{ km s}^{-1}$ (NED; Smith et al. 2000).

TABLE 5
SPECTRAL ANALYSIS REGIONS FOR THE CENTRAL 1.3 KPC OF NGC 4552

Region	Type	Shape	Center RA, DEC	Dimensions arcsec
R	source	annular	12 35 39.9, 12 33 23.4	11,17
R	background	annular	12 35 39.9, 12 33 23.4	20,31
NS	source	circular	12 35 39.8, 12 33 22.9	1.3
NS	background	annular	12 35 39.8, 12 33 22.9	1.6,3.2

NOTE.—WCS Coordinates for the centers of the regions are J2000. Dimensions specified are radii for circular regions, and (inner, outer) radii for annular regions. Region R is also shown Figure 2.

TABLE 6
SPECTRAL MODELS OF NGC 4552'S RINGS

kT keV	A Z_\odot	K 10^{-5} cgs	Λ 10^{-23} erg cm 3 s $^{-1}$	χ^2/dof
$^{\dagger} 0.64 \pm 0.02$	$0.7^{+0.4}_{-0.2}$	5.8	1.7	45.8/55
$0.65^{+0.02}_{-0.03}$	0.4	9.1	1.1	55/56
$0.64^{+0.03}_{-0.02}$	0.6	6.6	1.5	46.4/56
0.64 ± 0.02	0.8	5.1	1.9	46/56
0.64 ± 0.02	1.0	4.2	2.4	47.4/56

NOTE.—Spectral model parameters for the rings from region R (see Table 5 and Figure 2), using an absorbed single temperature APEC model fit over the 0.3 – 3 keV energy range. The spectrum contains 1840 net source counts. The hydrogen absorption column is fixed at the Galactic value ($n_{\text{H}} = 2.59 \times 10^{20} \text{ cm}^{-2}$). † The first row denotes the best fit model with temperature and abundance free to vary, while following rows hold the abundance fixed. Errors are 90% confidence limits.

TABLE 7
SPECTRAL MODELS OF THE NUCLEAR REGION OF NGC 4552

n_{H} 10^{20} cm^{-2}	kT keV	A Z_\odot	α	χ^2/dof
11 ± 4	2.2 ± 0.2	51.7/45
2.59^f	$1.04^{+0.13}_{-0.17}$	$0.5^{+0.9}_{-0.4}$	$1.7^{+0.2}_{-0.3}$	35.6/43
2.59^f	$1.04^{+0.21}_{-0.11}$	0.7^f	1.7 ± 0.1	35.7/44
< 6.7	$1.04^{+0.13}_{-0.18}$	0.7^f	1.7 ± 0.2	35.6/43

NOTE.—The spectrum contains 1046 net source counts in region NS, specified in Table 1, over the 0.3 – 5 keV band used for these fits. Superscript f denotes a fixed parameter. Errors are 90% confidence limits.